

Magnetic heating across the cosmological recombination era: Results from 3D MHD simulations

Pranjal Trivedi^{1,2*}, Johannes Reppin^{1†}, Jens Chluba^{3‡} and Robi Banerjee¹

¹Hamburger Sternwarte, University of Hamburg, Gojenbergsweg 112, 21029, Hamburg, Germany

²Department of Physics, Sri Venkateswara College, University of Delhi, 110021 New Delhi, India

³Jodrell Bank Centre for Astrophysics, Alan Turing Building, University of Manchester, Manchester M13 9PL, UK

ABSTRACT

The origin of cosmic magnetic fields is an unsolved problem and magnetogenesis could have occurred in the early Universe. We study the evolution of such primordial magnetic fields across the cosmological recombination epoch via 3D magnetohydrodynamic numerical simulations. We compute the effective or net heating rate of baryons due to decaying magnetic fields and its dependence on the magnetic field strength and spectral index. In the drag-dominated regime ($z \gtrsim 1500$), prior to recombination, we find no real heating is produced. Our simulations allow us to smoothly trace a new transition regime ($600 \lesssim z \lesssim 1500$), where magnetic energy decays, at first, into the kinetic energy of baryons. A turbulent velocity field is built up until it saturates, as the net heating rate rises from a low value at recombination to its peak towards the end of the transition regime. This is followed by a turbulent decay regime ($z \lesssim 600$) where magnetic energy dissipates via turbulent decay of both magnetic and velocity fields while net heating remains appreciable and declines slowly. Both the peak of the net heating rate and the onset of turbulent decay are delayed significantly beyond recombination, by up to 0.5 Myr (until $z \approx 600 - 700$), for scale-invariant magnetic fields. We provide analytic approximations and present numerical results for a range of field strengths and spectral indices, illustrating the redshift-dependence of dissipation and net heating rates. These can be used to study cosmic microwave background constraints on primordial magnetic fields.

Key words: cosmology:theory, early Universe, magnetic fields, magnetohydrodynamics, turbulence, cosmic background radiation

1 INTRODUCTION

Magnetic fields are observed ubiquitously and play an important role in the physics of galaxies out to large scales in the Universe (Beck 2015; Han 2017). Microgauss strength magnetic fields have also been detected in high redshift galaxies (e.g. Bernet et al. 2008; Kronberg et al. 2008; Mao et al. 2017) and across scales of several megaparsecs in clusters of galaxies (Clarke et al. 2001; Bonafede et al. 2010; Feretti et al. 2012). There is also indirect evidence from γ -ray observations suggesting a lower limit of $B \sim 10^{-16}$ G on intergalactic magnetic fields that can fill most of the cosmic volume (Neronov & Vovk 2010; Tavecchio et al. 2011; Dolag et al. 2011; Taylor et al. 2011; Dermer et al. 2011; Fermi-LAT Collaboration & Biteau 2018).

These observations motivate a primordial origin, i.e., from the very early Universe, for the seed magnetic field responsible for these observed large-scale fields. Theoretical models have been proposed for the generation of such a primordial magnetic field (PMF) which generically involves breaking of conformal invariance of the electromagnetic action. Primordial magnetogenesis could have occurred at inflation (Turner & Widrow 1988; Ra-

tra 1992; Gasperini et al. 1995; Martin & Yokoyama 2008; Subramanian 2010; Caprini & Sorbo 2014; Sharma et al. 2017) or at a cosmological phase transition (Vachaspati 1991; Sigl et al. 1997; Grasso & Rubinstein 2001; Copi et al. 2008). However, a complete theory of magnetogenesis and the PMF's subsequent evolution remains an important unresolved issue in cosmology (reviewed in Kandus et al. 2011; Durrer & Neronov 2013; Subramanian 2016).

The temperature and polarization anisotropies of the cosmic microwave background (CMB) are a sensitive probe of PMFs since magnetic fields induce metric perturbations as well as fluid perturbations via the Lorentz force (Subramanian 2006; Finelli et al. 2008; Paoletti et al. 2009; Shaw & Lewis 2010). Upper limits have been placed on the comoving PMF at megaparsec scales of order or just below $B \approx 1$ nG derived from comparison to *Planck* observations, based on the CMB power spectrum (Chluba et al. 2015; Planck Collaboration et al. 2016; Zucca et al. 2017) and CMB non-Gaussianity (Trivedi et al. 2012, 2014; Shiraishi & Sekiguchi 2014). Similar PMF upper limits exist from a range of other probes of magnetic fields including Faraday rotation of radio sources (Pshirkov et al. 2016) and changes to the cosmic ionization history (Sethi & Subramanian 2005; Kunze & Komatsu 2014, 2015; Chluba et al. 2015; Planck Collaboration et al. 2016).

However, a significant gap of several orders of magnitude between the upper limits and the inferred lower limits on large-scale

* E-mail: pranjal.trivedi@hs.uni-hamburg.de

† E-mail: johannes.reppin@hs.uni-hamburg.de

‡ E-mail: jens.chluba@manchester.ac.uk

primordial magnetic fields remains. Also, many of the currently applied approximations for magnetic heating and dissipation that are used to incorporate the effect on the cosmic ionization history, remain rather unsatisfactory (e.g., see discussions in [Chluba et al. 2015](#); [Planck Collaboration et al. 2016](#)). Thus, an improved understanding of PMF signatures is needed to clarify their current amplitude, evolution and origin. Motivated by the outstanding issues, we investigate the amount of decay and dissipation of a PMF and the resultant heating produced across the cosmological recombination era ([Zeldovich et al. 1968](#); [Peebles 1968](#); [Sunyaev & Chluba 2009](#)), one of the clearly anticipated phases in the evolution of PMFs.

PMFs are expected to evolve in a qualitatively distinct fashion across different cosmological epochs. Damping of PMFs can occur via neutrino- or photon-sourced fluid viscosity, via the development of magnetohydrodynamic (MHD) turbulent decay or processes such as ambipolar diffusion ([Jedamzik et al. 1998](#); [Subramanian & Barrow 1998](#); [Banerjee & Jedamzik 2004](#)).

Prior to cosmological recombination, there exists a photon drag-dominated viscous regime for the baryon-photon fluid. Close to the recombination epoch, once the radiation drag has started to drop abruptly, the PMF can source significant fluid motions. This induces turbulence in the baryon fluid which ultimately dissipates some fraction of the energy contained in the PMF via a turbulent cascade. The energy dissipated from the PMF can heat electrons and baryons to alter the thermal history ([Sethi & Subramanian 2005](#); [Kunze & Komatsu 2014, 2015](#); [Chluba et al. 2015](#)). We also note that a phase of MHD turbulent decay of the PMF can also occur subsequent to earlier phase transitions (eg. electroweak [Kahniashvili et al. \(2010\)](#)).

In this work, we report MHD simulations that describe the transfer and subsequent dissipation of magnetic energy across the epoch of recombination. Previous work has shown that turbulent decay will be important for PMF evolution after recombination ([Sethi & Subramanian 2005](#); [Chluba et al. 2015](#)). Here, using full 3D simulations, we are able to quantify both the sourcing of the velocity field, the development of turbulence and the decay of the PMF. Our simulations allow us to smoothly follow the PMF and baryon velocity field across three distinct regimes: the photon drag-dominated regime, a new transition regime around recombination and the post-recombination regime dominated by turbulent decay. In particular, we can trace the relatively rapid evolution of baryon velocities, magnetic fields and the heating rate (of baryons and electrons) due to magnetic decay during the transition regime. This enables us to connect the evolution of magnetic fields in the pre- and post-recombination epochs. We can then quantify the PMF decay and heating rate of the baryon fluid as a function of PMF parameters: amplitude and spectral index. The timescale for turbulence to develop after recombination also depends on the PMF parameters and this affects the epoch of peak heating caused by the PMF. The simulations and fits presented in this work refine our understanding of the evolution of the PMF and offer a way to potentially place improved constraints on the nature of primordial magnetic fields.

Quantifying the heating effect of PMF dissipation via decaying turbulence can be related to two further effects in the CMB caused by fluid heating. Heated electrons result in delayed recombination which in turn modifies the CMB power spectra ([Sethi & Subramanian 2005](#); [Chluba et al. 2015](#); [Kunze & Komatsu 2015](#)). Secondly, the additional energy in electrons up-scatters photons to higher energies, producing a distortion in the CMB spectrum ([Jedamzik et al. 2000](#); [Chluba & Sunyaev 2012](#)). These effects are important when placing improved constraints on the PMF and its origin. In addition, the effects of PMF dissipation and heating are

also relevant for assessing the role of the PMF in structure formation ([Wasserman 1978](#); [Kim et al. 1996](#); [Subramanian & Barrow 1998](#); [Sethi & Subramanian 2005](#)), 21-cm signals ([Sethi & Subramanian 2009](#); [Schleicher et al. 2009](#); [Shiraishi et al. 2014](#)), reionization signals ([Sethi & Subramanian 2009](#); [Bowman et al. 2018](#)) and primordial chemistry ([Schleicher et al. 2008b,a](#)), thus warranting careful treatments of the process. Our simulation outputs can also be used as initial conditions for the small-scale velocity field in structure formation simulations addressing the effects of PMFs.

The subsequent sections are organized in the following manner: In Section 2 we give a brief description of the magnetic field properties in the early Universe and present an overview of their evolution. In Section 3 we revisit the analytical treatment of the different evolutionary stages, specifically for the free-streaming damping epoch and the turbulent decay after recombination. The MHD simulations are described in Section 4, where we explain the numerical setup used to integrate the governing MHD equations and the techniques used for modeling the epoch of recombination. In Section 5 we present the results of the numerical simulations for magnetic field and velocity amplitudes, magnetic and kinetic power spectra and dissipation and net heating rates. Results are first described for the fiducial case with an initially near scale-invariant magnetic power spectrum. Subsequently, we present and analyze the trends in these physical results when varying the PMF parameters of the field amplitude and spectral index. We conclude the results section by providing a semi-analytical representation of the dissipation rate sourced by the decay of PMF in Section 5.3.4. A discussion of our results and caveats follows in Section 6 and conclusions are presented in Section 7

2 PRIMORDIAL STOCHASTIC MAGNETIC FIELD

We start by defining how the root mean square (rms) value of the primordial stochastic magnetic field (PMF) is related to the initial power spectrum at any moment. We assume that the initial power spectrum is given by $P_B(k) = Ak^{n_B}$, $n_B > -3$. Then the r.m.s. *comoving* magnetic field strength over some Gaussian filtering scale λ_f is related to

$$B_f^2 = a^4 \mathcal{B}_f^2 = \int \frac{d^3k}{(2\pi)^2} P_B(k) e^{-\lambda_f^2 k^2} = \frac{A \Gamma\left(\frac{n_B+3}{2}\right)}{4\pi^2 \lambda_f^{n_B+3}}, \quad (1)$$

where $\mathcal{B}_f^2 \propto (1+z)^4$ denotes the mean square field strength in proper coordinates. Equation (1) is simply a definition without any physical input at this point. For example, $\lambda_f = 1 \text{ Mpc}$ is frequently used to define B_λ at large cosmological scales (e.g., [Planck Collaboration et al. 2016](#)). One simple way to capture the evolution and damping of the rms magnetic field as a function of different epochs (e.g., for free-streaming damping) can be found by setting the filtering scale to $\lambda_f = \sqrt{2}/k_d(z)$, where k_d is a specified damping scale that depends on time. This is equivalent to saying that the initial power spectrum amplitude in Fourier space is modulated by a factor $\simeq e^{-2k^2/k_d^2(z)}$. We thus have

$$\bar{B}^2 = \frac{A \Gamma\left(\frac{n_B+3}{2}\right) k_d^{n_B+3}(z)}{4\pi^2 2^{(n_B+3)/2}}. \quad (2)$$

In this way, the rms magnetic field strength is determined by the evolution of $k_d(z)$. For near scale-invariant fields (e.g., $n_B = -2.9$), most of the energy is stored at the largest scales and even a significant evolution of k_d does not affect \bar{B}^2 very much. In contrast, for very blue initial PMF power spectra, most of the energy density is present at small scales and rapid loss is expected even if $k_d(z)$ only

evolves slowly. This simplified picture also provides a reasonable description of the magnetic field evolution in the turbulent decay phase, even if no exponential cut-off is expected at small scales, $k > k_d(z)$ (Jedamzik et al. 1998; Banerjee & Jedamzik 2004).

We will discuss below the evolution of the rms magnetic field strength across the recombination era in more detail. It is expected that in the phase well after recombination but before reionization ($10 \lesssim z \lesssim 10^3$) the magnetic field energy density changes relatively slowly (Banerjee & Jedamzik 2004). In this regime, *turbulent decay* of magnetic fields leads to a logarithmic evolution of the magnetic field strength with redshift. In particular for near scale-invariant initial power spectra, this implies a close to constant comoving magnetic field energy density, $\rho_B = a^{-4} \bar{B}^2 / 8\pi$.

For convenience, in our analytic treatment we will normalize all magnetic field power spectra with respect to the redshift at which turbulent decay is expected to begin in the post-recombination era, $z_{\text{id}} \approx 10^3$. We will determine z_{id} more precisely below, but with this definition we approximately have

$$\bar{B}^2 \approx B_0^2 \left(\frac{k_d(z)}{k_d} \right)^{n_B+3}, \quad (3)$$

with $B_0 \equiv \bar{B}(z_{\text{id}})$ and $k_d = k_d(z_{\text{id}})$. We now discuss the pre-recombination heating, which is dominated by free-streaming damping at $z \gtrsim z_{\text{id}}$, and the post-recombination heating separately, improving upon the previous treatments in the literature.

3 ANALYTICAL CONSIDERATIONS IN THE DIFFERENT REGIMES

The damping of magnetic fields and heating of the medium occurs in alternating phases of turbulent and viscous regimes (Jedamzik et al. 1998; Banerjee & Jedamzik 2004). In this section, we briefly recap and attempt to improve previous analytic approximations in the different eras. We start with the phase just before recombination and then discuss the turbulent decay regime in the post-recombination epoch ($z \lesssim 10^3$). These approximations are then compared with the numerical results in Sect. 5.

3.1 Free streaming damping

At sufficiently small scales (below the photon mean free path) and also at later redshifts after recombination, photons stream freely relative to the baryons. In this case, the baryon Alfvén speed, V_{bA} (in units of the light speed), in a magnetized medium is given by

$$\begin{aligned} V_{\text{bA}} &= \frac{a^{-2} \bar{B}}{\sqrt{4\pi\rho_b}} \equiv \sqrt{\frac{3}{2R}} \sqrt{\frac{\rho_B}{\rho_\gamma}} \approx \frac{3.8 \times 10^{-4}}{\sqrt{R}} \left[\frac{\bar{B}}{1 \text{ nG}} \right] \\ &\approx 1.5 \times 10^{-5} (1+z)^{1/2} \left[\frac{\Omega_b h^2}{0.022} \right]^{-1/2} \left[\frac{T_0}{2.726 \text{ K}} \right]^2 \left[\frac{\bar{B}}{1 \text{ nG}} \right] \\ R &= \frac{3\rho_b}{4\rho_\gamma} \approx \frac{666}{1+z} \left[\frac{\Omega_b h^2}{0.022} \right] \left[\frac{T_0}{2.726 \text{ K}} \right]^{-4} \\ \rho_B &= \frac{a^{-4} \bar{B}^2}{8\pi} \approx 9.5 \times 10^{-8} \left[\frac{\bar{B}}{1 \text{ nG}} \right]^2 \rho_\gamma \\ \rho_\gamma &\approx 0.26 \text{ eV cm}^{-3} \left[\frac{T_0}{2.726 \text{ K}} \right]^4 (1+z)^4, \end{aligned} \quad (4)$$

where \bar{B} is the rms magnetic field strength, R the baryon-loading of the fluid, ρ_B and ρ_γ the rms magnetic and photon energy densities respectively. The free-streaming photons exert a small drag

force, $\mathbf{F}_D \approx -\frac{4}{3} N_e \sigma_T \rho_\gamma \mathbf{v}$, on the baryons, mediated by the occasional scatterings of photons with the free electrons. This leads to damping of magnetic fields at very small scales¹, $\lambda \lesssim \lambda_{\text{fs}}$. These interactions source small-scale photon perturbations, which gradually damp due to free-streaming mixing (e.g., see Minoda et al. 2017, for recent study of generation of small-scale fluctuations by PMFs in clusters).

3.2 Estimates for the free-streaming scale

The free-streaming scale is approximately determined by the condition (Subramanian 2016)

$$\frac{1}{k_{\text{fs}}^2} \approx \int \frac{V_{\text{bA}}^2 R dt}{N_e \sigma_T a^2} \approx 1.4 \times 10^{-7} \left[\frac{B_0}{1 \text{ nG}} \right]^2 \int \left(\frac{k_{\text{fs}}}{k_d} \right)^{n_B+3} \frac{dt}{N_e \sigma_T a^2}, \quad (5)$$

where the baryon Alfvén speed, V_{bA} , baryon loading factor of the fluid, R , and magnetic energy density, ρ_B , defined in Eq. (4) give $V_{\text{bA}}^2 R = 3\rho_B / 2\rho_\gamma$. For convenience we introduce the integral

$$\frac{1}{k_\lambda^2} = \int_0^t \frac{dt'}{N_e \sigma_T a^2} = \int_z^\infty \frac{dz}{N_e \sigma_T a H(z)}, \quad (6)$$

which can be computed numerically and only depends on the standard background cosmology. It is approximately given by (see Fig. 1), $k_\lambda \approx \sqrt{8/45} k_D$, where the standard photon diffusion damping scale, k_D , is defined by (Weinberg 1971; Kaiser 1983)

$$\frac{1}{k_D^2} \approx \frac{8}{45} \int_z^\infty \frac{dz}{N_e \sigma_T a H} \left[\frac{1}{1+R} + \frac{15}{16} \frac{R^2}{(1+R)^2} \right], \quad (7)$$

for shear viscosity $\eta_\gamma = \frac{16}{45} \frac{\rho_\gamma}{N_e \sigma_T}$, which includes the effect of polarization². We have $k_D \approx 4.1 \times 10^{-6} (1+z)^{3/2} \text{ Mpc}^{-1}$ in radiation-dominated era, such that $k_\lambda \approx 1.8 \times 10^{-6} (1+z)^{3/2} \text{ Mpc}^{-1}$. In the matter-dominated regime, one has $k_\lambda \propto (1+z)^{5/4}$, however, in our computation we use the full numerical result, which captures the rapid changes of k_D and k_λ around $z \approx 10^3$ (Fig. 1).

By separating variables in Eq. (5) and solving for k_{fs} we obtain

$$\begin{aligned} k_{\text{fs}} &\approx k_d \left(1.4 \times 10^{-7} \frac{(n_B+5)}{2} \left[\frac{B_0}{1 \text{ nG}} \frac{k_d}{k_\lambda} \right]^2 \right)^{-\frac{1}{n_B+5}} = k_d \left[\frac{k_\lambda}{k_\lambda(z_{\text{id}})} \right]^{\frac{2}{n_B+5}} \\ k_d &= \sqrt{\frac{2}{n_B+5}} \frac{k_\lambda(z_{\text{id}})}{3.8 \times 10^{-4}} \left[\frac{B_0}{1 \text{ nG}} \right]^{-1}, \end{aligned} \quad (8)$$

where we used $k_{\text{fs}} \approx k_d$ at z_{id} . Usually, the time-dependence of k_{fs}/k_d is omitted, such that the factor $(k_{\text{fs}}/k_d)^{n_B+3}$ in Eq. (5) can taken outside the integral. This yields a slightly different solution

$$\begin{aligned} k_{\text{fs}}^* &\approx k_d^* \left(1.4 \times 10^{-7} \left[\frac{B_0}{1 \text{ nG}} \frac{k_d^*}{k_\lambda} \right]^2 \right)^{-\frac{1}{n_B+5}} = k_d^* \left[\frac{k_\lambda}{k_\lambda(z_{\text{id}})} \right]^{\frac{2}{n_B+5}} \\ k_d^* &= \frac{k_\lambda(z_{\text{id}})}{3.8 \times 10^{-4}} \left[\frac{B_0}{1 \text{ nG}} \right]^{-1}, \end{aligned} \quad (9)$$

which does not include any dependence of k_{fs} and k_d on the PMF spectral index. To fix k_{fs} we still need to estimate z_{id} . However, it is already clear that $z_{\text{id}} \approx 10^3$, thus, $k_\lambda(z_{\text{id}}) \approx 0.01 - 0.1 \text{ Mpc}^{-1}$, which puts us into the regime $k_d \approx 26 - 260 \text{ Mpc}^{-1}$ for $n_B \approx -3$ and $B_0 \approx 1 \text{ nG}$. Due to resolution issues and to avoid shocks, in our simulations we are only able to treat fields with $B_0 \lesssim 10^{-2} \text{ nG}$. Assuming $B_0 = 10^{-2} \text{ nG}$, one thus expects $k_d \approx 2600 - 26000 \text{ Mpc}^{-1}$. We will see that in fact the lower end of this range seems to be reproduced by the simulations (cf. Fig. 6).

¹ We denote comoving scales with λ and proper scales with $\ell = a\lambda$.

² Without this effect one has $\eta = \frac{4}{15} \frac{\rho_\gamma}{N_e \sigma_T}$ (Weinberg 1971).

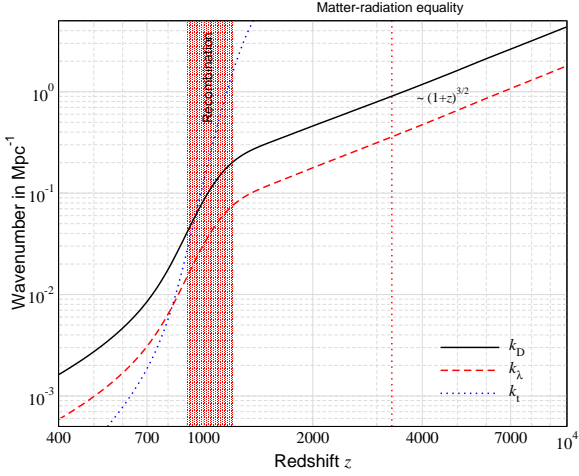


Figure 1. Illustration for redshift dependence of some of the relevant scales. Here, k_D and k_λ are defined by Eq. (6) and (7), respectively. We also introduced $k_t = 2\pi N_e \sigma_T a / \sqrt{R}$ for convenience.

3.2.1 Estimate for z_{id}

To determine the redshift z_{id} at which the turbulent decay resumes after recombination, we use the condition that the kinetic Reynolds number should be $R_e \simeq 1$ at $k_{\text{fs}} \approx k_{\text{id}}$ and then $R_e > 1$ afterwards. In the free streaming regime, we have $R_e \approx V_{\text{bA}} R / \alpha_\gamma \ell_{\text{fs}} \approx V_{\text{bA}} R \ell_{\text{mfp}} / \ell_{\text{fs}}$, where the drag coefficient $\alpha_\gamma \approx N_e \sigma_T / R$ and $\ell_{\text{mfp}} = 1 / N_e \sigma_T$ for the mean free path were used (Banerjee & Jedamzik 2004; Subramanian 2016). With $\ell_{\text{fs}} = \lambda_{\text{fs}} a = 2\pi a / k_{\text{fs}}$, this yields³ the condition

$$\int_{z_{\text{id}}}^{\infty} \frac{dz}{N_e \sigma_T a H(z)} \approx \frac{2}{(n_B + 5)} \frac{R}{(2\pi N_e \sigma_T a)^2} \Big|_{z_{\text{id}}}, \quad (10)$$

for the redshift z_{id} . We also define $k_t = 2\pi N_e \sigma_T a / \sqrt{R}$, such that Eq. (10) can be cast into the form $k_\lambda(z_{\text{id}}) \approx \sqrt{(n_B + 5)/2} k_t(z_{\text{id}})$.

In Fig. 1, we show a comparison of the different wave numbers relevant to the discussion. The solution of Eq. (10) in our treatment here is independent of the magnetic field strength. For $n_B = -3$, we find $z_{\text{id}} \approx 820$ and more generally

$$z_{\text{id}} \approx 820 \left[1 - 4.66 \times 10^{-2} (n_B + 3) + 1.39 \times 10^{-3} (n_B + 3)^2 \right] \quad (11)$$

for $n_B \in [-3, 3]$ to percent precision. This shows that in our treatment z_{id} drops gradually with increasing spectral index, n_B . We furthermore obtain

$$k_\lambda(z_{\text{id}}) \approx 7.50 \times 10^{-3} \text{ Mpc}^{-1} [1 - 0.295 (n_B + 3) + 4.66 \times 10^{-2} (n_B + 3)^2 - 2.97 \times 10^{-3} (n_B + 3)^3], \quad (12)$$

which determines k_{id} in Eq. (8). This shows a moderate dependence of k_{id} on n_B , giving $k_{\text{id}} \approx 20 \text{ Mpc}^{-1} [B_0/1 \text{ nG}]^{-1}$ for $n_B \approx -3$ to $k_{\text{id}} \approx 3.3 \text{ Mpc}^{-1} [B_0/1 \text{ nG}]^{-1}$ for $n_B \approx 2$ in our treatment. We will see below that both Eq. (11) and Eq. (12) do not capture the dependence of the turbulent regime on B_0 and n_B , in particular when increasing n_B (see Sect. 5.2 and Sect. 5.3).

Comparing our results to previous works, a value $k_{\text{id}} \approx 200 - 300 \text{ Mpc}^{-1} [B_0/1 \text{ nG}]^{-1}$ is usually quoted (e.g., Sethi & Subramanian 2005; Kunze & Komatsu 2015; Subramanian 2016). Also, the redshift for turbulent decay usually is set to $z_{\text{id}} \approx 1100$ (e.g., Sethi

& Subramanian 2005; Kunze & Komatsu 2015), independent of the PMF spectral index or strength. Here, we find lower values in both cases. The main reason for the different value at $n_B \approx -3$ is the factor of 2π in the conversion from λ_{fs} to k_{fs} . This yields the modified condition, $k_\lambda(z_{\text{id}}) \approx k_t(z_{\text{id}})/2\pi$, for z_{id} , which due to the exponential dependence of k_λ and k_t on redshift (see Fig. 1) results in $z_{\text{id}} \approx 1050$ instead. Overall, our simulations seem to suggest a scaling $k_{\text{id}} \approx 20 \text{ Mpc}^{-1} [B_0/1 \text{ nG}]^{-1}$ and $z_{\text{id}} \approx 800$ in agreement with our simple analytic estimate for $n_B = -3$.

3.2.2 Magnetic field dissipation in the pre-recombination era

The wavenumber k_{id} is only relevant if we wish to compare the initial power spectrum amplitude, A , for different values of B_0 and n_B . By construction, we already ensured that at $z = z_{\text{id}}$ we have $\bar{B}^2 \approx B_0^2$ for all n_B . However, for different n_B the effective damping scale at z_{id} differs, so that also the respective values for A at the initial time vary. Consequently, we can also write

$$\bar{B}^2 \approx B_0^2 \left(\frac{k_{\text{fs}}(z)}{k_{\text{id}}} \right)^{n_B+3} = B_0^2 \left(\frac{k_\lambda(z)}{k_\lambda(z_{\text{id}})} \right)^{2(n_B+3)/(n_B+5)} \quad (13)$$

at $z \gtrsim z_{\text{id}}$, where we used Eq. (8) to eliminate $k_{\text{fs}}(z)/k_{\text{id}}$. We then have the magnetic dissipation rate⁴ at $z \gtrsim z_{\text{id}}$

$$\frac{d(Q_B/\rho_\gamma)}{dz} \approx \frac{2(n_B+3)}{n_B+5} \frac{\rho_B}{\rho_\gamma} \frac{\partial_z k_\lambda(z)}{k_\lambda(z)} = \frac{(n_B+3)}{n_B+5} \frac{k_\lambda^2(z) r_B(z)}{N_e \sigma_T a H}, \quad (14)$$

where we used $-(1/2)k_\lambda^2 \partial_z k_\lambda^{-2} = k_\lambda^{-1} \partial_z k_\lambda$ and the magnetic energy density fraction $r_B(z) = \rho_B(z)/\rho_\gamma(z)$.

In the radiation-dominated era, $\rho_B(z) \propto \rho_\gamma(z) k_\lambda^{2(n_B+3)/(n_B+5)}$ and $k_\lambda \approx 1.8 \times 10^{-6} (1+z)^{3/2} \text{ Mpc}^{-1}$ such that we find the redshift scaling $dQ_B/dz \propto \rho_\gamma(z) (1+z)^{2(n_B+2)/(n_B+5)}$. This is in excellent agreement with previous studies (Banerjee & Jedamzik 2004; Wagstaff & Banerjee 2015), but differs slightly from Kunze & Komatsu (2014), who obtained $dQ_B/dz \propto \rho_\gamma(z) (1+z)^{(3n_B+7)/2}$. The difference is because $k_{\text{fs}} \propto k_D \propto (1+z)^{3/2}$ was used in their expression, which neglects the scaling of k_{fs} because of changes in ρ_B . For blue magnetic field power spectra, this overestimates the free-streaming heating, as also pointed out by Wagstaff & Banerjee (2015).

To compare with our numerical simulations, it is furthermore useful to give the scaling in the matter-dominated regime. Then $k_\lambda \propto (1+z)^{5/4}$ and $H \propto (1+z)^{3/2}$, such that one has $dQ_B/dz \propto \rho_\gamma(z) (1+z)^{(3n_B+5)/2(n_B+5)}$. This shows a slightly slower increase with redshift than for the radiation-dominated case. Our simulations reveal a scaling trend for magnetic dissipation which is similar and this is discussed in Sect. 5.3.4 with reference to Fig. 18.

3.2.3 Creation of spectral distortions in the drag regime

In the drag-dominated phase, the dissipated magnetic field energy flows directly to the CMB photons, as these provide the viscosity in the free-streaming era. This causes a small y -distortion (Jedamzik et al. 2000; Sethi & Subramanian 2005; Wagstaff & Banerjee 2015), which physically is due to photon mixing (Chluba et al. 2012), and also sources CMB temperature anisotropies at ultra-small scales ($k \gtrsim 20 \text{ Mpc}^{-1} [B_0/1 \text{ nG}]^{-1}$). Since we are in the free-streaming regime, the photon mixing process is *incomplete* so that only a (small) fraction of the magnetic field energy really creates a distortion. This is in stark contrast to the damping of primordial temperature fluctuation that erases all small-scale fluctuation

³ We use $R_e^2 = 1$ to readily eliminate B_0 from the expression.

⁴ For this we need to compute $-a^{-4} d(a^4 \rho_B)/dt = -\rho_\gamma(z) d(\rho_B/\rho_\gamma)/dt$.

due to photon diffusion, which allows $\approx 1/3$ of the acoustic wave energy to create an all-sky average distortion (Chluba et al. 2012).

We also highlight that a small y -distortion has no significant effect on the baryon temperature and the recombination history as long as it remains below the *COBE/FIRAS* limit (Chluba & Sunyaev 2009). Thus, this part of the PMF dissipation can only be constrained by measuring CMB spectral distortions and ultra small-scale CMB anisotropies, in spite of opposing recent claims (Kunze 2017). Simple estimates, assuming that all the energy creates distortions, suggest a Compton y -parameter, $y \approx 10^{-8} - 10^{-7}$, for $B_0 \approx 1$ nG (Wagstaff & Banerjee 2015). Due to the finite resolution of the beam, which essentially leads to mixing of blackbodies of different temperature and hence a distortion (Chluba & Sunyaev 2004), these estimates provide useful upper limits; however, since many other sources of y -distortions at similar or larger level exist (e.g., Refregier & et al. 2000; Chluba & Sunyaev 2012; Hill et al. 2015), it will be hard to use future distortion measurements to improve existing PMF limits in this way.

3.3 Turbulent decay after recombination

In this section, we briefly recap the analytic approximations commonly used to describe the heating in the turbulent decay regime. We then provide an improved derivation that also includes the evolution of the magnetic field strength on the eddy turnover time. These approximations will be used later to represent the results from our numerical simulations (e.g., Sect. 5.3.4).

3.3.1 Review of previous analytical results

As argued by Banerjee & Jedamzik (2004), in the post-recombination era turbulent decay dominates the damping of the magnetic field energy density with a evolution law

$$E_B(z) \approx E_{B,\text{td}} \left[\frac{t}{t_{\text{eddy}}} \right]^{-2(n_B+3)/(n_B+5)} \quad (15)$$

for $t \gg t_{\text{eddy}}$. Here, t_{eddy} is the eddy turnover time of the largest turbulent mode at the initial time, $t_{\text{td}} = t(z_{\text{td}})$, and $E_B = |B|^2/8\pi = a^4 \rho_B$ is the corresponding comoving magnetic energy density.

How do we generalize this to the expanding Universe? First of all, we want to obtain the limit $t \rightarrow t_{\text{td}}$ for which $E_B(z) \rightarrow E_{B,\text{td}}$. Sethi & Subramanian (2005) suggested the generalization as

$$E_B(z) \approx E_{B,\text{td}} \left[1 + \frac{t - t_{\text{td}}}{t_{\text{eddy}}} \right]^{-m} \quad (16)$$

with $m = 2(n_B+3)/(n_B+5)$, which indeed has the right limit towards $t \rightarrow t_{\text{td}}$. In the expanding Universe one also needs to replace

$$\frac{t - t_{\text{td}}}{t_{\text{eddy}}} \rightarrow \int \frac{dt}{t_{\text{eddy}}} = \frac{1}{[t_{\text{eddy}} H]_{\text{td}}} \int_z^{z_{\text{td}}} \frac{dz}{1+z} = \frac{1}{\tau_{\text{td}}} \ln \left(\frac{1+z_{\text{td}}}{1+z} \right). \quad (17)$$

Here, we have taken into account the explicit redshift dependence of the eddy turnover time, $t_{\text{eddy}}(z) \approx \ell_{\text{eddy}}/v_{\text{bA}} \approx t_{\text{eddy}}(z_{\text{td}}) (a/a_{\text{td}})^{3/2}$, using $v_{\text{bA}} \propto a^{-1/2}$ and $\ell_{\text{eddy}} \propto a$, and assumed $H \propto a^{-3/2}$ as appropriate for the matter-dominated era. This neglects any evolution of v_{bA} related to ρ_B . We also defined $\tau_{\text{td}} = t_{\text{eddy}}(z_{\text{td}})H(z_{\text{td}})$, which is $\tau_{\text{td}} \approx [RH/(N_e \sigma_{\text{T}} c)]_{\text{td}} \approx 0.063$ by construction. We thus obtain

$$E_B(z) \approx E_{B,\text{td}} \left[1 + \frac{1}{\tau_{\text{td}}} \ln \left(\frac{1+z_{\text{td}}}{1+z} \right) \right]^{-m}, \quad (18)$$

which agrees well with previously used expressions (cf., Sethi &

Subramanian 2005). With this we find the dissipation rate at $z \lesssim z_{\text{td}}$

$$\frac{d(Q_B/\rho_\gamma)}{dz} \approx -\frac{1}{(1+z)} \frac{m}{\tau_{\text{td}}} \frac{r_{B,\text{td}}}{\left[1 + \frac{1}{\tau_{\text{td}}} \ln \left(\frac{1+z_{\text{td}}}{1+z} \right) \right]^{m+1}}, \quad (19)$$

which is usually used to describe the heating due to turbulent decay. Notice, that in contrast to the heating in the free-streaming regime, this term directly affects the baryons, raising their temperature and thus leading to changes of the cosmological recombination history.

3.3.2 Phenomenological derivation for the turbulent decay law

The picture for decay of magnetic fields in the turbulent phase is that the time-scale on which energy is drained is given by the eddy turnover time around the critical scale that defines the comoving energy density of the fields, $E_B = |B|^2/8\pi = a^4 \rho_B$. From Eq. (2) it follows that $\lambda_c \propto E_B^{-1/(n_B+3)}$. We then have

$$\frac{1}{t_{\text{eddy}}} \approx \frac{v_{\text{bA}}}{\lambda_c a} \approx \frac{1}{t_{\text{eddy,td}}} \left(\frac{E_B}{E_{B,\text{td}}} \right)^{1/m} \left(\frac{a}{a_{\text{td}}} \right)^{-3/2}, \quad (20)$$

where we used $v_{\text{bA}} \propto \sqrt{E_B/R}$ and set $m = 2(n_B+3)/(n_B+5)$ as before. We normalized everything with respect to the values at z_{td} . Then the evolution equation for the comoving magnetic energy density is given by

$$\frac{dE_B}{dt} \approx -\frac{E_B}{t_{\text{eddy}}} = -\frac{E_B}{t_{\text{eddy,td}}} \left(\frac{E_B}{E_{B,\text{td}}} \right)^{1/m} \left(\frac{a_{\text{td}}}{a} \right)^{3/2} = -\frac{E_B^{(m+1)/m}}{\tau_{\text{eddy,td}} a^{3/2}} \quad (21)$$

with $\tau_{\text{eddy,td}} = t_{\text{eddy,td}} E_{B,\text{td}}^{1/m} a_{\text{td}}^{-3/2}$. Neglecting the expansion of the Universe, we can set $a = a_{\text{td}}$ and then integrate from t_{td} to find

$$E_B(t) \approx E_{B,\text{td}} \left[1 + \frac{t - t_{\text{td}}}{m t_{\text{eddy,td}}} \right]^{-m}, \quad (22)$$

which is only valid for $n_B > -3$. Comparing with Eq. (16), shows that solution is a little different, with an extra factor $1/m$ modulating the eddy turnover time, which we will discuss below.

Now including the effect of expansion during the matter-dominated era yields

$$E_B(t) \approx E_{B,\text{td}} \left[1 + \frac{1}{m \tau_{\text{td}}} \ln \left(\frac{1+z_{\text{td}}}{1+z} \right) \right]^{-m} \quad (23)$$

in a similar manner. Comparing with Eq. (18), we can see that again an extra factor of $1/m$ appears. Taking the redshift derivative yields

$$\frac{d(Q_B/\rho_\gamma)}{dz} \approx -\frac{1}{(1+z)} \frac{1}{\tau_{\text{td}}} \frac{r_{B,\text{td}}}{\left[1 + \frac{1}{m \tau_{\text{td}}} \ln \left(\frac{1+z_{\text{td}}}{1+z} \right) \right]^{m+1}} \quad (24)$$

for the magnetic dissipation rate in the turbulent decay regime. As we can see, the heating amplitude differs by $1/m$ with respect to Eq. (19) and scales slightly faster with redshift for near scale invariant initial spectra, since we have $m \rightarrow 0$ for $n_B \rightarrow -3$.

Does the extra factor of $1/m$ in the evolution law make sense? For blue initial power spectra, the energy density is fully dominated by the smallest scales. For $n_B \rightarrow \infty$, we find $m \rightarrow 2$, so that the evolution law, Eq. (22), becomes

$$E_B(t) \approx E_{B,\text{td}} \left[1 + \frac{t}{2 t_{\text{eddy,td}}} \right]^{-m}. \quad (25)$$

This indicates that the relevant time for energy dissipation is about twice the eddy turnaround time, a result that is also found in typical turbulent flow simulations. For lower values of n_B , the evolution affects the total energy density of the magnetic fields to a smaller extent and the eddy turnover time also scales less strongly with

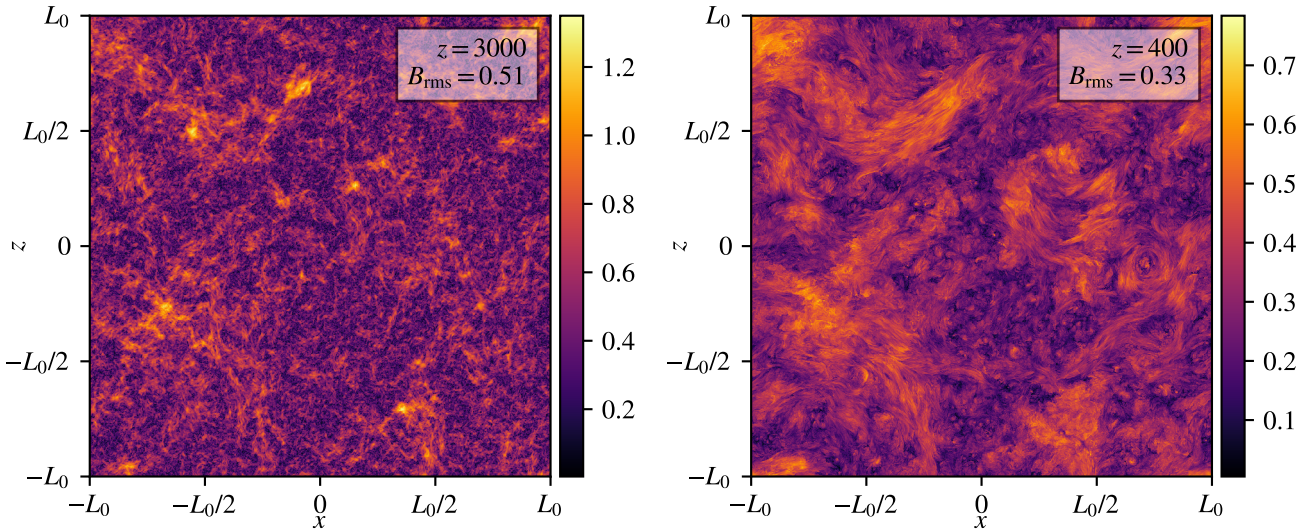


Figure 2. Slices representing the magnetic field strength absolute value $|B| = \sqrt{B_x^2 + B_y^2 + B_z^2}$ through the $x - z$ plane at $y = 0$ in the simulation box at two different redshifts, near the beginning of the simulation, at $z = 3000$ (left panel) and near the end, at $z = 400$ (right panel). The fields shown are for the fiducial case $n_B = -2.9$ and $B_0 = 0.51$ with both $|B|$ and B_{rms} expressed in code units of Alfvén velocity divided by sound speed. Note the lower intensity scale for the evolved magnetic field strength at $z = 400$.

time. In the limit of quasi-constant strength of fields at all scales ($n_B \approx -3$), we also have $t_{\text{eddy}}(E_B) \approx \text{const}$, which means that the field strength decays exponentially at a rate $1/t_{\text{eddy}}$. This limit is more problematic, since in this case the true small-scale dissipation time-scale, t_{turb} , will determine the rate of change of the energy density and not the time-scale at which energy is injected into the turbulent cascade ($\approx t_{\text{eddy}}$). However, for $n_B > -3$ our approximate model should still provide a reasonable description of the problem in the different regimes, as long as $t_{\text{eddy}} \gg t_{\text{turb}}$.

A last argument why the factor $1/m$ seems appropriate is that we know that at the initial redshift z_{id} we should find

$$\begin{aligned} \frac{d(Q_B/\rho_\gamma)_{\text{id}}}{dz} &\equiv \frac{1}{[H(1+z)]_{\text{id}}} \frac{da^4 \rho_B(z_{\text{id}})}{a^4 dt} \approx -\frac{1}{[H(1+z)]_{\text{id}}} \frac{r_{B,\text{id}}}{t_{\text{eddy},\text{id}}} \\ &= -\frac{r_{B,\text{id}}}{(1+z_{\text{id}})\tau_{\text{id}}}, \end{aligned} \quad (26)$$

as is directly obtained from Eq. (24) for $z = z_{\text{id}}$ but is *not* reproduced by the law in Eq. (19). This shows that the magnetic dissipation rate at the transition from free-streaming damping to turbulent decay for fixed $\rho_B(z_{\text{id}})$ is independent of n_B .

We will use Eq. (24) as a starting point for analytic representations of our numerical results. Even if it does not capture the physics completely, it does represent the late time evolution very well (see Fig. 18). Together with Eq. (14) for the pre-recombination evolution, we obtain a very useful semi-analytic description over a wide range of PMF parameters (also see Sect. 5.3.4).

4 SIMULATIONS OF HEATING BY PRIMORDIAL MAGNETIC FIELDS

In this section, we describe the setup of our numerical magneto-hydrodynamic (MHD) simulations to follow the evolution of cosmological magnetic and velocity fields from the photon drag dominated regime, across the recombination era, into the turbulent decay dominated regime. Our goal is to compute and follow the evolution

of the net heating produced by the dissipation of magnetic energy. We first detail the numerical methods, the code employed, the form of the MHD equations and the integration scheme used. The choice of cosmological coordinates and initial conditions is then described and the evolution of the photon drag is presented. Conversion to physical units is also discussed. We then briefly discuss how to use the results to extract different dissipation and heating rates.

4.1 Numerical Method and Setup

4.1.1 The Pencil-Code

We perform full 3-D simulations with the *Pencil-Code* (Brandenburg & Dobler 2010), at a resolution of $N = 1536^3$, to numerically investigate the details of heating and sourcing of turbulence by magnetic fields in the context of varying photon viscosity across the epoch of recombination. Two-dimensional slices of the simulated 3D magnetic and baryon velocity fields, near the start and end epochs, are shown in Figs. 2 & 3 and discussed in section 5.1.1.

The *Pencil-Code* is a finite-differences code with a sixth-order integration scheme. It solves the equations that govern the flow of the plasma and its interactions with the magnetic field for every grid point individually using the values of three neighbouring cells for the derivatives. This method means we are limited to subsonic velocities and sub-sonic Alfvén velocities, which limits us to a physical magnetic field strength $B_{\text{phys}} \lesssim \text{few} \times 10^{-2} \text{ nG}$ (Sect. 4.1.4). In general, the density fluctuations are of the order $\approx 1\%$, corresponding to (nearly) incompressible flows.

The code integrates the MHD equations in the following form,

$$\frac{D \ln \rho}{Dt} = -\nabla \cdot \mathbf{u} \quad (27a)$$

$$\frac{D \mathbf{u}}{Dt} = -\frac{\nabla p}{\rho} + \frac{\mathbf{j} \times \mathbf{B}}{\rho} + \mathbf{f}_{\text{visc}} \quad (27b)$$

$$\frac{\partial \mathbf{A}}{\partial t} = \mathbf{u} \times \mathbf{B} - \eta \mathbf{j}, \quad (27c)$$

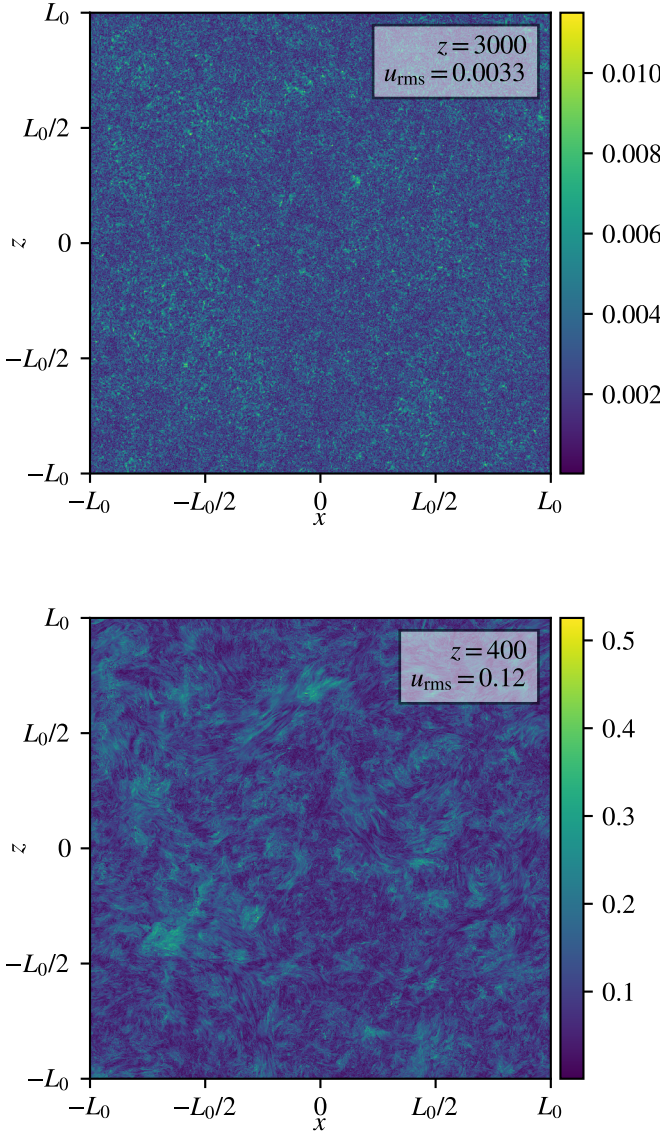


Figure 3. Slices representing the baryon velocity absolute value $|u| = \sqrt{u_x^2 + u_y^2 + u_z^2}$ through the $x-z$ plane at $y = 0$ in the simulation box at two different redshifts, $z = 3000$ (upper panel) and $z = 400$ (lower panel). Both $|u|$ and u_{rms} are in code units (i.e. divided by sound speed). Note the 50 times smaller intensity scale for $|u|$ at $z = 3000$.

where $D/Dt = \partial/\partial t + \mathbf{u} \cdot \nabla$ is the convective derivative, ρ describes the (mass) density, \mathbf{u} the velocity field of the plasma and $\mathbf{j} = \nabla \times \mathbf{B}$ is the MHD current in the simulation. Equation (27a) is the continuity equation of the plasma, Eq. (27b) is the Navier-Stokes equation, and Eq. (27c) is the induction equation of the magnetic field.

There also is a magnetic resistivity η in the code, meaning we are working with *non-ideal* MHD. It is set in such a way that the magnetic Prandtl number, the ratio of viscosity to resistivity, is given by $\text{Pr} = \nu_3/\eta_3 = 1$. The code uses the vector potential \mathbf{A} , with $\mathbf{B} = \nabla \times \mathbf{A}$ as a primitive variable, as it naturally ensures the divergence free condition $\nabla \cdot \mathbf{B}$ for the magnetic field.

We do not explicitly solve the energy equation in our simulation, since we use an isothermal equation of state where the pressure

is only dependent on the density in the simulation with $p = c_s^2 \rho$. Assuming a mono-atomic gas of particles, the sound speed is then given (e.g. Ma & Bertschinger 1995) by $c_s = \sqrt{4/3 k_B T_b/m_p} \approx 5.7 \text{ km s}^{-1} [(1+z)/1100]^{1/2}$. We also assume a post-recombination neutral hydrogen gas in thermal equilibrium with the CMB photon field, $T_b \approx T_\gamma \propto a^{-1}$, which is valid until $z \lesssim 150$. At scales below the photon diffusion scale (most relevant to our problem), the expression employed for the sound speed is valid even in the pre-recombination era, as photons and baryons no longer behave as a single tightly-coupled fluid ($c_s = c/\sqrt{3}$) in the free-streaming regime (see Jedamzik et al. 1998; Banerjee & Jedamzik 2004, for a more detailed discussion). At larger scales, corrections could become relevant, but the effect of damping is deemed negligible at those scales. We also neglect the effect of recombination on the sound speed, which is related to the change in the number of free particles. For instance, for a fully ionized electron-proton plasma, one would have⁵ $c_s^{\text{ep}} \approx \sqrt{2} c_s \approx 1.4 c_s$.

The last term in Eq. (27b) describes the viscosity of the baryon-photon fluid. It includes the effect of photon drag, which we model as a viscosity acting on the fluid, and additional numerical viscosity to avoid numerical instabilities, as well as to mimic sub-grid dissipation effects in the fully turbulent regime:

$$\mathbf{f}_{\text{visc}} = \mathbf{f}_{\text{hyper}} + \mathbf{f}_{\text{drag}} \quad (28)$$

$$\mathbf{f}_{\text{hyper}} = \nu_3 \nabla^6 \mathbf{u} \quad (29)$$

$$\mathbf{f}_{\text{drag}} = -\alpha(z) \cdot \mathbf{u}. \quad (30)$$

The effect of numerical viscosity $\mathbf{f}_{\text{hyper}}$ is controlled by the variable ν_3 , which we optimize to avoid large pile-up of power at small-scales in the turbulent phase (see Sect. 4.1.6 and App. A for a detailed discussion of convergence w.r.t. numerical viscosity in our simulations). We discuss the implementation of the photon drag term $\alpha(z)$ in Sect. 4.1.3. Our simulations neglect all gravitational interactions of the plasma as well as any contributions from photon perturbations.

4.1.2 Transformation to Cosmological Coordinates

The `Pencil-Code` works in dimensionless code units, with time expressed in units of the Hubble time, assuming the matter-dominated regime, $t_{\text{exp}} = H^{-1} = t_0 a^{3/2} \approx 8.2 \times 10^{17} (h/0.7)^{-1} a^{3/2} \text{ s}$. Here, we do not explicitly treat the radiation-dominated regime, which only changes the redshift-dependence of the drag-dominated dissipation rate (see Sect. 3.2.2). We furthermore use the *super-comoving* coordinates (Banerjee & Jedamzik 2004):

$$\tilde{\rho}_b = a^3 \rho_b \quad \tilde{p} = a^4 p \quad \tilde{\mathbf{B}} = a^2 \mathbf{B} \quad \tilde{\mathbf{u}} = a^{1/2} \mathbf{u} \quad (31a)$$

$$d\tilde{t} = dt/t_{\text{exp}} \quad \tilde{\eta} = a^{-1/2} \eta \quad \tilde{\mathbf{A}} = a \mathbf{A} \quad \tilde{\mathbf{j}} = a^{7/2} \mathbf{j}. \quad (31b)$$

This coordinate transformation is a rescaling that uses the conformal property of the MHD equations allowing us to describe MHD in an expanding FRW Universe via the form of the MHD equations in a flat spacetime (see Eq. 27). Only one additional term is introduced, a kinematic Hubble drag described in the next subsection. Within the simulation, the comoving sound speed $\tilde{c}_s = 1$, so that computational velocities or magnetic field amplitudes can be converted to physical units using $\mathbf{v} = c_s \tilde{\mathbf{u}}$ and $\mathbf{B} = \sqrt{4\pi \rho_b} c_s \tilde{\mathbf{u}}_\Lambda$, where $\tilde{\mathbf{u}}_\Lambda$ is the Alfvén velocity obtained directly from the code. To map from \tilde{t} to redshift, we use $d\tilde{t} = dt/t_{\text{exp}} \equiv -d \ln(1+z)$, where

⁵ The more general expression should read $c_s^2 \approx \frac{4}{3}(1-Y_p)(1+f_{\text{He}}+X_e) \frac{k T_b}{m_p}$, where $f_{\text{He}} \approx 0.079$ for $Y_p = 0.24$ and $T_b \approx T_\gamma \propto a^{-1}$.

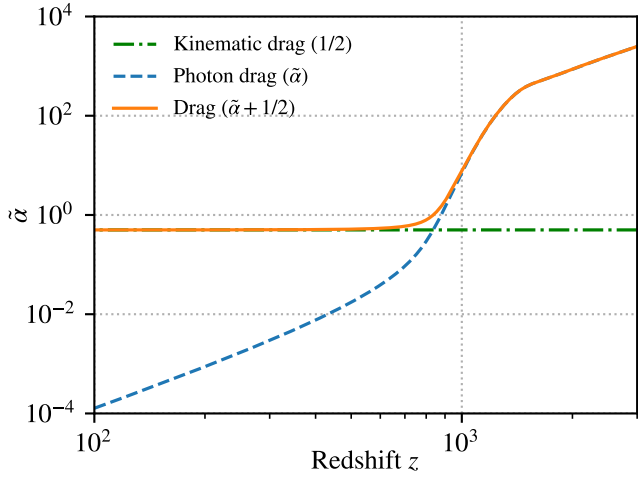


Figure 4. The evolution of the photon drag coefficient $\tilde{\alpha}$, Eq. (33), in the simulation code units (where rates are in units of Hubble rate) as well as the constant kinematic drag coefficient $H/2$ (or $1/2$ in code units), which is important only at late epochs.

$dt = -t_{\text{exp}} a dz$. We obtain $\tilde{t} = \ln[(1+z_0)/(1+z)]$, where z_0 is the starting redshift. This implies $(1+z) = (1+z_0)e^{-\tilde{t}}$, which is then used to compute the evolving photon drag coefficient $\alpha(z)$.

4.1.3 Photon Drag

The occasional scattering of photons off electrons in the free-streaming regime damps magnetic field power at small scales (Jedamzik et al. 1998). In physical units, the drag coefficient is given by (e.g., Banerjee & Jedamzik 2004)

$$\alpha = \frac{c}{R\ell_{\text{mfp}}} = \frac{\sigma_{\text{T}}N_{\text{e}}c}{R} = \frac{\sigma_{\text{T}}N_{\text{H}}c}{R} X_{\text{e}}, \quad (32)$$

where $N_{\text{H}} \approx 1.9 \times 10^{-7} (1+z)^3 \text{ cm}^{-3}$ is the hydrogen nuclei number density⁶ and X_{e} the free electron fraction, which is provided by CosmoRec (Chluba & Thomas 2011). The time transformation $dt \rightarrow d\tilde{t}$, implies that the rescaled drag coefficient is $\tilde{\alpha} = t_{\text{exp}}\alpha$, relevant in the computation. Inserting numerical values then yields

$$\tilde{\alpha} \approx 4.6 \times 10^{-6} \left[\frac{\Omega_{\text{m}} h^2}{0.14} \right]^{-1/2} \left[\frac{T_0}{2.726 \text{ K}} \right]^4 X_{\text{e}} (1+z)^{5/2}, \quad (33)$$

where $\Omega_{\text{m}} h^2$ sets the total matter density. The evolution of $\tilde{\alpha}$ is illustrated in Fig. 4. At $z \gg 1100$, the photon drag is dominant and prevents turbulence from developing. As recombination proceeds, the drag coefficient drops quickly and the flow becomes turbulent (also see discussion of the magnetic Reynolds number cf. Fig. 10).

In the final form of the velocity equation (27b), an extra kinematic drag term $-\frac{1}{2}Hu$ appears due to our choice of scalings corresponding to an expanding Universe (cf. Banerjee & Jedamzik 2004). This term is usually neglected; however, it becomes significant after recombination (see Fig. 4) and can be incorporated by replacing $\tilde{\alpha} \rightarrow \tilde{\alpha} + \frac{1}{2}$ inside the code. In the computation of the net heating rate, this term has to be taken into account as it reduces the net heating rate noticeably.

⁶ Assuming helium fraction $Y_{\text{p}} = 0.24$.

4.1.4 Physical Units

To convert our code units into physical units, we use the physical sound speed $c_{\text{s}} \approx 5.7 \text{ km s}^{-1} [(1+z)/1100]^{1/2}$ at recombination, evaluated at the current epoch $c_{\text{s}} \approx 0.17 \text{ km s}^{-1} (1+z)^{1/2}$ as a comoving sound speed. We assume $T_{\text{e}} = T_{\text{y}} \propto (1+z)$ at all times. This approximation is valid in the standard recombination scenario until $z \approx 150$; however, significant heating by magnetic fields could change this, an effect that we do not treat in our simulations.

We can then determine the comoving physical box size using the distance an Alfvén wave travels within a Hubble time t_0 . Taking the Alfvén speed equal to the plasma sound speed gives a box size $L_{\text{phys}} \approx t_0 c_{\text{s}} L_{\text{code}} \approx 28 (h/0.7)^{-1} \text{ kpc}$, where $L_{\text{code}} = 2\pi$ for our simulation box. The wavenumber in physical units then can be calculated from the box size, $L_{\text{phys}} \approx 2\pi/k_{\text{phys}}$ yielding $k_{\text{phys}} \approx 220 (h/0.7) \text{ Mpc}^{-1}$. For the smallest resolved physical scale, we therefore have $k_{\text{res}} \approx (N/2)k_{\text{phys}} \approx 1.7 \times 10^5 (h/0.7) \text{ Mpc}^{-1}$ with a typical number of grid points $N = 1536$.

The magnetic field strength from an Alfvén velocity equivalent to the sound speed is given by $B_{\text{phys}} = \sqrt{4\pi\rho_{\text{b}}} c_{\text{s}} \approx 3.9 \times 10^{-2} \text{ nG}$. To avoid the requirement of including significant density perturbations and shocks, we must limit Alfvén velocities to $v_{\text{bA}} \lesssim c_{\text{s}}/2$. Thus, for the simulations considered here (and presented in the subsequent figures) the comoving physical magnetic field strengths lie in the range $B_{0,\text{phys}} \approx (0.086 - 2.0) \times 10^{-2} \text{ nG}$, corresponding to Alfvén velocities in the range $\approx (0.022 - 0.51) c_{\text{s}}$.

4.1.5 Initial Conditions

In our simulations, we initialize the magnetic field with a specific power spectrum $P_M \propto k^n$ with a spectral index n , recalling that $n = n_{\text{B}} + 2$. This is done by initializing a Gaussian random field in k -space which is then multiplied with the chosen power-law and transformed back into real space. By doing this we also have full control over the helicity of the magnetic field $\mathcal{H} = \mathbf{A} \cdot \mathbf{B}$, which we set to zero at the initial epoch, focusing on non-helical fields. Since magnetic helicity is a conserved quantity (although strictly, only in ideal MHD) this remains constant for the entire simulation, except for numerical fluctuations. By choosing the amplitude of the magnetic power spectrum we can fix the B_{rms} in our simulation. This is also discussed in Sect. 2 (where magnetic power spectrum was denoted as $P_B(k)$ and the spectral index n_{B} differs by two: $n = n_{\text{B}} + 2$).

The velocity field is initialized with $\mathbf{u}|_{t=0} = 0$. After a few time steps velocity fluctuations of the order $u_{\text{max}} \approx c_{\text{s}}$ develop, which then damp out. This *ring-in* phase is usually restricted to the high redshifts $z \sim 5000$, but for very steep spectra or low magnetic field strengths, it can last until $z \approx 3000$. We show our results and figures for times $z \leq 3000$, after this phase has ended and the simulation has gone into a near steady state. Unless stated otherwise, we keep track of the evolution of the magnetic and velocity field during the initial phase and rescale our curves to their values at $z = 3000$, taking that epoch as the relevant initial condition for physical interpretation.

4.1.6 Numerical viscosity and real heating

We use the hyperviscosity implementation of the Pencil-Code since it gives the lowest numerical dissipation and largest Reynolds numbers in the simulation. A small amount of numerical viscosity is required but we do not want it to be stronger than the physical effects we wish to observe and follow. For a given resolution

one can use a specific minimum viscosity pre-factor ν_3 . To further reduce this pre-factor, one has to increase the resolution N . For a given viscosity, ν_3 , the simulation is independent of resolution as long as one is above the minimum value of the viscosity, which is a function of resolution. On the other hand there must exist enough dissipation when the photon drag becomes negligible. A detailed discussion of how the viscosity pre-factor was chosen as well as the convergence tests of resolution can be found in App. A. The adopted value of $\nu_3 = 2.5 \times 10^{-16}$ is used in all the studies below where when no explicit viscosity parameter values are mentioned.

4.2 Theoretical considerations for magnetic heating rates

In our simulations, the PMFs are the origin of energy that can subsequently be dissipated. Physically, the PMFs drive baryon velocities through the Lorentz force, sourcing a kinetic energy density, $\rho_{\text{kin}} = \frac{1}{2} \rho_b \langle v_b^2 \rangle$. This process builds up a flow, which itself loses energy through i) interactions with CMB photons (via photon drag) and ii) dissipative processes at ultra-small scales (via Coulomb interactions and plasma effects). Photon drag leads to small-scale perturbations in the photon temperature, which through photon mixing processes can cause y -type distortions (see Sect. 3.2.3). The dissipative processes at ultra-small scales lead to heating of the baryons, which becomes important in the turbulent phase of the evolution.

Neglecting dissipation processes, the total (comoving) energy density⁷, $E_{\text{tot}} = E_B + E_{\text{kin}}$, related to magnetic fields is conserved. Here, $E_B = a^4 \rho_B \equiv \frac{1}{2} a^4 \rho_b \langle v_{A,b}^2 \rangle$ and $E_{\text{kin}} = a^4 \rho_{\text{kin}} = \frac{1}{2} a^4 \rho_b \langle v_b^2 \rangle$. Real changes to the total energy are then given by

$$\frac{dE_{\text{tot}}}{dt} = \frac{dE_B}{dt} + \frac{dE_{\text{kin}}}{dt} = -2\alpha E_{\text{kin}} - HE_{\text{kin}} - \left. \frac{dE_{\text{tot}}}{dt} \right|_{\text{heat}}. \quad (34)$$

The first term on the r.h.s. is due to photon drag, which can be obtained as $\dot{E}_{\text{kin|drag}} \simeq \frac{1}{2} a^4 \rho_b \langle 2v_b v_b \rangle \equiv -2\alpha E_{\text{kin}}$ using $\dot{v}_b = -\alpha v_b$. The second term is related to the extra cooling from Hubble expansion. This term causes extra losses from the velocity field and has to be eliminated when computing the net heating rates. The last term is due to dissipative processes in the baryon plasma at ultra-small scales, which leads to real heating.

Around the recombination era, three phases exist: at redshift $z \gg z_{\text{id}}$, the dissipation is dominated by photon drag, so that

$$\frac{dE_{\text{tot}}}{dt} \approx -2\alpha E_{\text{kin}}. \quad (35)$$

As is clear from Fig. 4, the Hubble term can be neglected here. In this phase, *no real heating occurs*, but perturbations in the photon fluid are generated at small scales through the Doppler effect. In this regime the drag is so strong that only very small velocity fluctuations are generated by magnetic fields (via the Lorentz force). The drag is strong enough to prevent magnetic fields from accelerating baryons up to the Alfvén-velocity, such that turbulence is highly suppressed (see Sect. 5 and Fig. 5).

Around $z \simeq z_{\text{id}} \simeq 10^3$, hydrogen atoms form and photon drag drops rapidly. The velocity field slowly builds up until a turbulent flow is formed. However, in the transition phase, little energy is actually dissipated, and most of the energy lost by the PMFs is dumped to increase the flow's kinetic energy (see Fig. 5).

In the turbulent phase ($z \lesssim z_{\text{id}}$), photon drag can be neglected

and a significant fraction of the energy lost from the magnetic fields is converted into heat by the turbulent cascade:

$$\frac{dE_{\text{tot}}}{dt} \approx -HE_{\text{kin}} - \left. \frac{dE_{\text{tot}}}{dt} \right|_{\text{heat}}. \quad (36)$$

In the simulations, we can thus compute the real heating of the medium in the various phases as

$$\left. \frac{dE_{\text{tot}}}{dt} \right|_{\text{heat}} \approx -\frac{dE_B}{dt} - \frac{dE_{\text{kin}}}{dt} - HE_{\text{kin}} - 2\alpha E_{\text{kin}}. \quad (37)$$

We will see below that the above picture is reproduced by the simulations. In particular, the transition phase between the drag-dominated and the turbulent regime is a new physical regime that was previously missing or treated as unrealistically abrupt.

4.2.1 Extraction of heating rates from simulation

Within our simulations, the scales responsible for real heating of the medium (due to Coulomb interactions) are not resolved but instead mimicked by numerical viscosity to reproduce a quasi-Kolmogorov turbulent cascade with magnetic field power spectrum similar to $E_k \propto k^{-5/3}$ (see Sect. 4.1.6). To compute the total energy loss rate of the PMFs, we can use the definition of the Alfvén speed, V_{bA} , Eq. (4) for the ratio of the average magnetic to photon energy density. This yields

$$\langle r_B \rangle = \frac{\langle \rho_B \rangle}{\rho_\gamma} = \frac{2R}{3} \langle V_{bA}^2 \rangle = \frac{2R}{3} \frac{c_s^2}{c^2} \langle \tilde{u}_A^2 \rangle, \quad (38)$$

where we used $V_{bA}^2 = (c_s^2/c^2) \tilde{u}_A^2$. We recall that \tilde{u}_A is the Alfvén velocity obtained directly from the code. Noting that $R \propto a$ and $c_s^2 \propto a^{-1}$, we can then compute the dissipation and heating rates in physical units in terms of the rate of change of Alfvén velocity \tilde{u}_A or magnetic field amplitude B_0 , both squared, and both in the same code units,

$$\begin{aligned} \frac{d(Q_B/\rho_\gamma)}{d \ln z} &= -\frac{d \langle r_B \rangle}{d \ln z} \approx -1.4 \times 10^{-10} \frac{d}{d \ln z} \langle \tilde{u}_A^2 \rangle \\ &\approx -3.7 \times 10^{-11} \frac{d}{d \ln z} \left(\left(\frac{B_0}{0.51} \right)^2 \right), \end{aligned} \quad (39)$$

where $c_s^2/c^2 \simeq 3.2 \times 10^{-13}(1+z)$ and the value $B_0 = 0.51$ corresponds to our fiducial case. Note that the magnetic dissipation rate $dQ_B/d \ln z$ or $dE_{\text{mag}}/d \ln z$ in Fig. 7 is the negative rate of change of magnetic energy density $d(\rho_B)/d \ln z$. Similarly, we can define the changes to the kinetic energy density of the fluid and net heating rates through Eq. (37).

5 SIMULATION RESULTS FOR DIFFERENT PMF PARAMETERS

The subsequent sections describe our results for the evolution of the amplitudes and power spectra of both magnetic and velocity fields as well as for the derived dissipation and heating rates. Initially, we present simulation results for a single value of magnetic field strength, chosen with a near scale-invariant magnetic power spectrum (Sect. 5.1). Subsequently, we discuss results for varying magnetic field amplitude as well as varying magnetic spectral index (Sect. 5.2 and 5.3). We also compare our results with analytical expressions, highlighting expected trends and differences, providing analytic fits where relevant.

⁷ The photon energy density is not affected significantly and will be assumed to remain unaltered throughout the evolution.

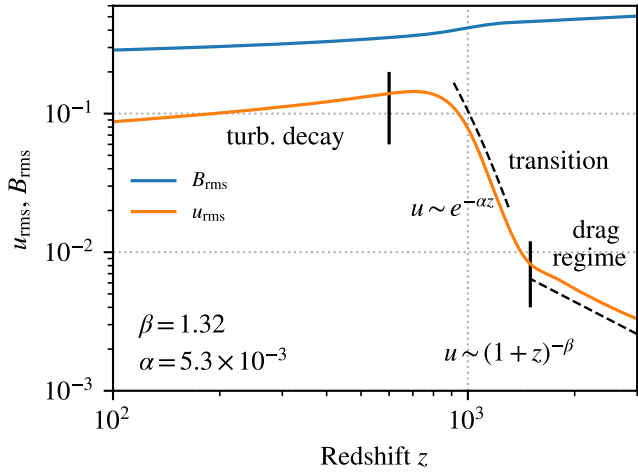


Figure 5. Evolution of the r.m.s. amplitudes (in code units, i.e. relative to the sound speed) of the magnetic field B_{rms} and baryon velocity field u_{rms} for the fiducial case of a near scale-invariant magnetic power spectrum with amplitude $B_0 = 0.51$ at $z = 3000$ (corresponding to $B_{0,\text{phys}} \approx 2.0 \times 10^{-2}$ nG).

5.1 Scale-invariant magnetic spectrum

We first present simulation results for a single fiducial case with magnetic field amplitude $B_0 = 0.51$ (in code units of v_A/c_s) at $z = 3000$. This field amplitude is equivalent to $B_{0,\text{phys}} \approx 2.0 \times 10^{-2}$ nG. This fiducial case is chosen for a nearly scale-invariant power spectrum $n_B = -2.9$ (or alternatively, $n = n_B + 2 = -0.9$), which is of particular importance in the study of primordial magnetic fields generated by inflation.

5.1.1 Evolution of magnetic and kinetic amplitude

A visual representation of the changing magnetic field strength and baryon velocity over 2D slices from our 3D simulations is shown in Figs. 2 & 3. A video of the temporal evolution of both the magnetic and kinetic field intensity slices can also be viewed at <https://www.hs.uni-hamburg.de/research/cosmo-mf>. Note the varying intensity scale between $z = 3000$ $z = 400$, particularly for the velocity in Fig. 3. We can clearly see how the magnetic field decays slowly before recombination, evolves quicker over the transition regime and then spatially mixes and decays in the turbulent regime. The velocity field is boosted from zero initial value to saturation toward the end of the transition regime and subsequently exhibits turbulent mixing and decay.

To analyze the evolution of the magnetic and kinetic energy density over the course of our simulation, we plot the root mean square (rms) velocity and magnetic field strength in Fig. 5. At higher redshifts prior to decoupling, the fluid is dominated by photon drag. During this drag dominated regime, there is little evolution of the magnetic field – it decreases by less than 10% from its early value of $B_0 = 0.51$ at $z = 3000$. The kinetic field, initially starting from zero, is still highly suppressed, by more than two orders of magnitude compared to the sound speed c_s , at $z = 3000$. It then rises slowly from $u_{\text{rms}} \approx 1.5 \times 10^{-3}$ to 5×10^{-3} at $z \approx 1500$ as the drag coefficient decreases (see Fig. 4 where the drag is shown separately). We fit this slower rise of the velocity field with a power law $u \sim (1+z)^{-\beta}$, with $\beta = 1.32$.

Below a redshift of $z \sim 1400$, the transition regime sets in due to a sharp decrease in the photon drag (Fig. 5). For this period

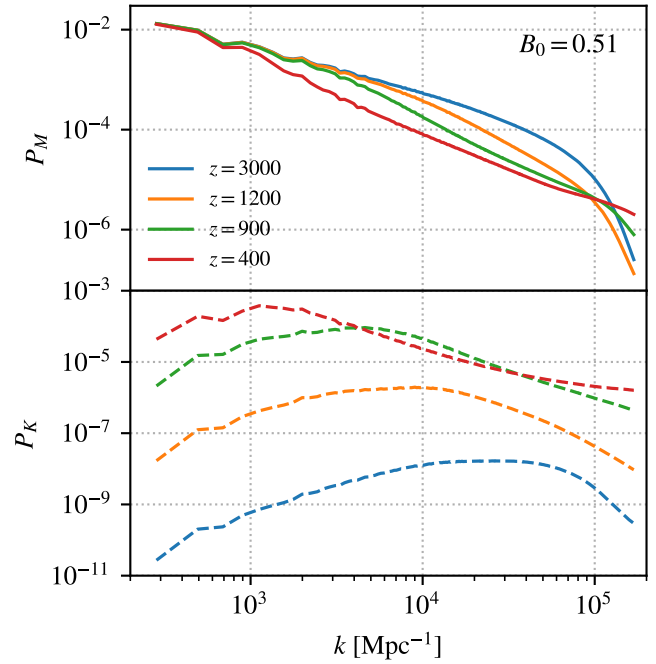


Figure 6. Evolution of magnetic (solid lines) and kinetic (dashed lines) power spectra versus redshift for a scale-invariant initial magnetic field. Spectra are shown for early times $z = 3000$, during the transition regime at $z = 1200$ & 900 , and once the fluid has become fully turbulent at $z = 400$. The magnetic field strength is $B_0 = 0.51 \Leftrightarrow B_{0,\text{phys}} = 2.0 \times 10^{-2}$ nG at the reference redshift $z = 3000$

we fitted the steep increase in the velocity field amplitude with an exponential function $u \sim e^{-\alpha z}$ yielding a value of $\alpha = 5.4 \times 10^{-3}$. This transition regime lasts until the velocity to magnetic field ratio approaches a maximum value of $u_{\text{rms}}/B_{\text{rms}} \approx 1/2$. However, actual equipartition, which one could expect, is not reached and could be related to the fields' intermittent nature over the total volume (Subramanian 1998; Federrath et al. 2011). This is also similar to the departure from full equipartition observed in earlier simulations of turbulence with the Pencil-Code (e.g., Reppin & Banerjee 2017).

At $z \approx 800$ turbulent decay starts to set in, leading to the continued dissipation of the magnetic field energy as well as a turnover and then gradual decrease in the kinetic energy of the baryon velocity field. During the turbulent period, the r.m.s. magnetic field strength further decreases such that by $z = 100$ it is approximately 60% of its original value at $z = 3000$. This can be seen more clearly in the upper panel of Fig. 8. The transition phase captured in our simulations introduces a significant delay in the onset of turbulence.

5.1.2 Magnetic and kinetic power spectra

In Fig. 6 (upper panel), we show the magnetic power spectra P_M for different redshifts in our simulation for an initial near scale-invariant magnetic field ($n = -0.9$ or $n_B = -2.9$). The power spectrum P_M is defined to be v_A^2 integrated over the angular variables in configuration space. The total energy of the magnetic field can be computed as the integral of the power spectrum in k -space, $E = \int P_M dk = \int k P_M d \ln k$ and one can also define an integral scale k_I . For a scale-invariant spectrum we have $P_M \propto k^{-0.9}$ and the integral scale in our simulation is the box size L . For the more blue cases, $P_M \propto k^n$, $n = 0, 1, 2$ the integral scale k_I is at larger k , a little closer to the Nyquist wavenumber in the simulation.

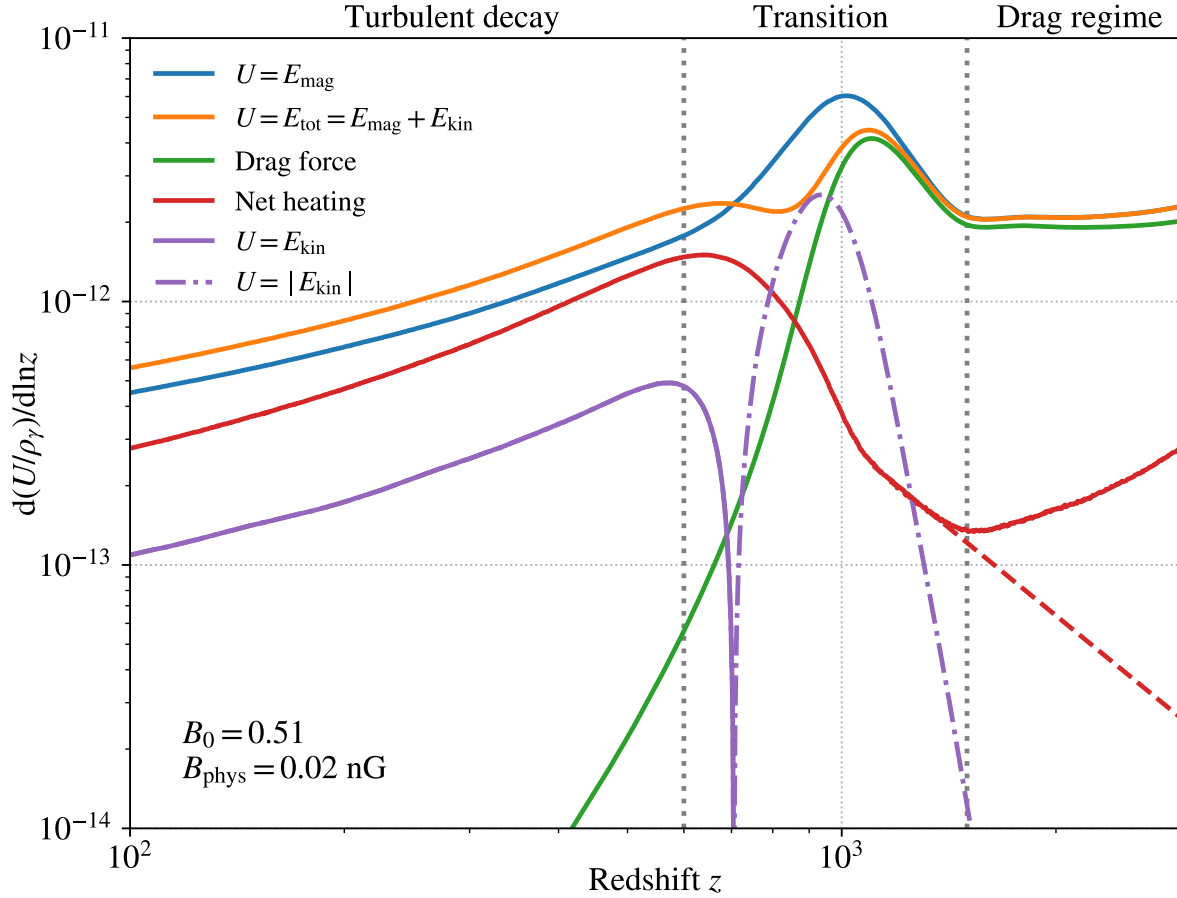


Figure 7. Energy density dissipation rates and the net heating rate (red curve) for the simulation fiducial case with a near scale-invariant spectrum $E_k \approx k^{-0.9}$, normalized to the radiation energy density. The net heating rate is computed via $[dE_{\text{tot}}/d\ln z - 2(\bar{\alpha} + 1/2)E_{\text{kin}}]/\rho_\gamma$ (Eq. 37). The dashed red line shows the extrapolation of the effective heating rate for $\nu_3 \rightarrow 0$, derived from Fig. A2. The green curve shows the rate of change of magnetic and kinetic energy density using Eq. (39). The blue and purple curves show the rate of change of magnetic and kinetic energy density using Eq. (39). The dash-dot purple line shows the negative part of the kinetic energy density dissipation rate, when the kinetic velocity field is gaining energy from the magnetic field. As the net heating rate excludes the contribution from the kinematic drag term, it does not add up to the total energy dissipation rate.

For the magnetic power spectra, shown in Fig. 6, the first spectrum is plotted at $z = 3000$, when the ring-in phase for velocities has already ended. The spectrum follows a power-law $P_M \propto k^{-0.9}$ up to the high- k regime. The small-scale fluctuations have been damped out and the spectrum has a steep decline towards the Nyquist wavenumber $k_{\text{Ny}} = N/2$, where N is the resolution. Close to the Nyquist scale, the magnetic power spectrum has an exponential cutoff with the shape $P_M \propto e^{-2k^2/k_d^2}$, with the dissipation scale k_d (Jedamzik et al. 1998; Subramanian 2016)

We observe that the power spectrum is slowly reshaped during the transition period, as visible for $z=1200$ and 900 . This is because the ionization fraction decreases and the drag force on the baryons becomes negligible. The scale-invariant initial spectrum is transformed into a broken power-law spectrum with a knee below which it is steeper. In the turbulent phase ($z \lesssim 800$), this knee, where the $k^{-0.9}$ spectrum turns into a turbulent one, moves to smaller k over time, which means ever larger scales become turbulent in the simulation. Also, due to the negligible drag force at $z \lesssim 800$, the viscosity becomes dominated by the small hyperviscosity we added to the simulation setup. This has the effect of extending the spectrum more and more towards the Nyquist scale k_{Ny} and reducing the strong exponential cutoff which is apparent in the earliest spec-

trum shown at $z = 3000$. At the latest redshift shown, $z = 400$, the fluid has become fully turbulent at the scales present in our simulation with the power spectrum steepened to an almost Kolmogorov spectrum (with an energy distributed as $E \propto k^{-5/3}$), though in our simulations we find a power-law exponent of ≈ -1.44 , slightly flatter than the canonical value.

The kinetic power spectrum evolves in a clearly different manner (see the lower panel of Fig. 6). We start our simulation with zero initial velocity $\mathbf{u}_0 = 0$ and the first power spectrum of the kinetic field at $z = 3000$ is during an epoch, when the fluid is heavily dominated by photon drag. At this epoch only a small fraction of the total energy is in the velocity field, so the power spectrum is approximately two orders of magnitude below the magnetic power spectrum. The kinetic power spectrum is peaked at a very large wavenumber, $k_{\text{peak,phys}} \approx 4 \times 10^4 (h/0.7) \text{ Mpc}^{-1}$.

During the transition period a stronger kinetic power spectrum develops. It has a roughly $E_k \propto k^2$ shape until it reaches its peak, which shifts to lower k as the kinetic power spectrum builds up. At wave numbers larger than the peak, there is a turbulent spectrum, with $E_k \propto k^{-5/3}$. By $z = 900$, the slope of the turbulent part of the power spectrum is found to be -1.71 . At the final redshift, $z = 400$, the slope becomes slightly flatter than Kolmogorov due to a small

bottleneck effect at the highest k -values (as tuning of hyperviscosity ν_3 was done for the *magnetic* power spectrum). As the ionization fraction decreases and becomes negligible, the turbulent part of the spectrum covers a wider range of scales, starting from lower and lower k -values. Towards the end of the simulation, $z = 400$, this scale is at $k \approx 1000 (h/0.7) \text{ Mpc}^{-1}$. A video of the temporal evolution of both the magnetic and kinetic spectra can be viewed at <https://www.hs.uni-hamburg.de/research/cosmo-mf>.

5.1.3 Energy dissipation rates and net heating

In Fig. 7, we show the dissipation rate, i.e. the negative rate of change, per logarithmic redshift, of the magnetic energy density $dE_{\text{mag}}/d \ln z$ (blue curve) calculated using Eq. (39). Also shown are the dissipation rates of the kinetic energy density (purple), total ($E_{\text{mag}} + E_{\text{kin}}$) energy density (orange), the photon drag force (per unit area) $2\tilde{\alpha}E_{\text{kin}}$ (green), and finally the difference between the total energy dissipation rate and the drag rate, which can be interpreted as the *net heating rate* being imparted into the fluid (red curve). Note that the kinematic drag term, related to the Hubble expansion, $-(1/2)H\mathbf{u}$, is subtracted out from the net heating and not shown as included in the drag curve (green). At high redshifts we also show the expected net heating rate (red dashed) if we had very low viscosity at $z > 1500$, taken from extrapolation from the net heating behaviour for lower ν_3 shown in Fig. A2.

In Fig. 7, one can clearly identify the three stages discussed above: at early times, the net heating is very small and energy losses from the magnetic fields are created by the effect of photon drag. Starting from $z \approx 1500$, baryon velocities build up, absorbing losses from the magnetic fields, until a turbulent flow is formed. Once turbulence develops below $z \sim 700$, the velocity field starts losing energy via a turbulent cascade. Net heating is observed to gradually build up once baryon velocities start rising. The rise becomes faster as the drag decreases. Then the net heating peaks as the transition era gives way to turbulent decay, and net heating decreases throughout the turbulent phase down to low redshifts.

For the chosen fiducial case initial conditions, the magnetic energy dissipation rate peaks around recombination at a redshift of about $z \approx 1000$, whereas the net heating rate peaks at $z \approx 600$. This significant delay ($\sim 0.5 \text{ Myr}$) is caused by the time taken for the fluid to transition into the turbulent state. The net heating rate has a broad distribution and is not a sharply peaked feature as was expected from earlier analytical studies. This means that the onset of modifications to the cosmological ionization history are expected to be more gradual, which will avoid numerical issues pointed out in Chluba et al. (2015).

Note that the magnetic energy dissipation rate curve lies above the total energy dissipation rate up until a redshift of $z \approx 700$. This is because up until then the kinetic energy density increases, adding a negative contribution (dot-dashed purple curve) to the total energy dissipation rate. At late times, both magnetic and kinetic fields decay turbulently, contributing positively to the total energy dissipation rate $dE_{\text{tot}}/d \ln z$. In this turbulent phase, the real losses from the system lead to heating of matter.

5.2 Variation of magnetic amplitude

In this section we present simulation results for a varying magnetic field amplitude over the range $B_0 = (0.022 - 0.51)$ corresponding to $B_{0,\text{phys}} \approx (0.086 - 2.0) \times 10^{-2} \text{ nG}$, investigating the behaviour of magnetic and kinetic amplitudes as well as dissipation and net heating rates as a function of varying B_0 .

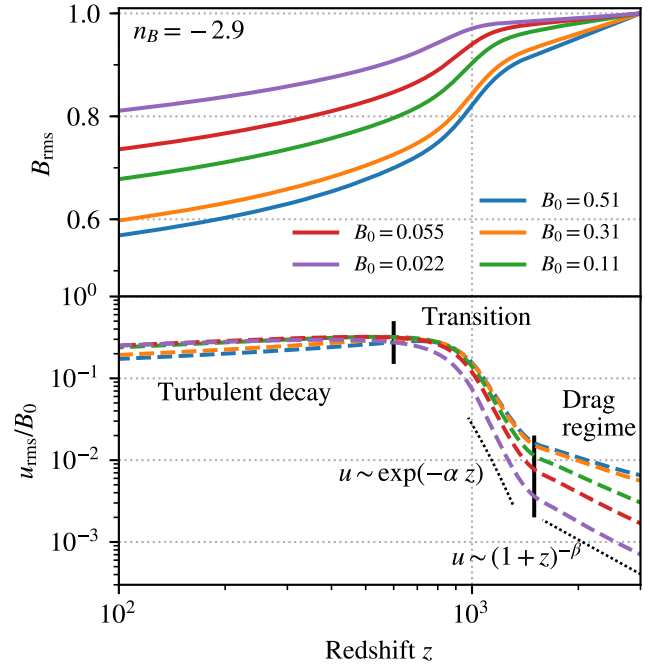


Figure 8. Evolution of magnetic (top) and kinetic (bottom) field r.m.s. amplitudes versus redshift for different initial magnetic field strengths B_0 . The initial field strength was varied by a factor of ≈ 20 (values denoted in the legend) and the magnetic amplitudes are all normalized to unity at $z = 3000$. Velocities are rescaled to the magnetic field strengths B_{rms} .

5.2.1 Evolution of magnetic and kinetic amplitude

In Fig. 8 we show different simulation runs with varying initial ($z = 3000$) magnetic field strength amplitude B_0 . The upper panel shows the evolution of the magnetic field strength B_{rms} on a linear vertical scale. The lower panel shows the velocity field strength u_{rms} , rescaled to the magnetic field strength B_{rms} , on a logarithmic vertical scale. For the lowest initial field strength $B_0 = 0.022$ there is a 20% decrease of the initial rms field value over the entire redshift range $3000 > z > 100$ that goes into increasing the velocity field. This diminution or decay of magnetic fields becomes more appreciable reaching $\approx 45\%$ for the strongest magnetic field case $B_0 = 0.51$, highlighting that turbulent time-scales become shorter with increasing magnetic field strength.

As we first observed for the fiducial case, we again see three distinct phases from the simulation results for different initial amplitudes. The first one is the drag dominated regime, where $u_{\text{rms}} \ll 1$ (i.e., $v \ll v_{\text{BA}}$). From the upper panel of Fig. 8, where $B_{\text{rms}}(z)$ is depicted, we see that for the lower B_0 runs, much less than a percent of magnetic field energy is transferred to u_{rms} during the drag dominated phase $3000 > z > 1500$, whereas it is $\sim 1\%$ for the highest B_0 case. The u_{rms} amplitude (plotted in units of initial B_0) is an increasing function of the initial amplitude B_0 in the drag regime. The stronger the initial magnetic field amplitude B_0 , the more energy is transferred to the velocity field, albeit at a relatively small fraction. In the subsequent transition regime, B_{rms} values decay most rapidly while the velocities rise more sharply, both effects due to the decreasing drag. However, by the end of the transition phase all curves catch up to reach a similar ratio of $u_{\text{rms}}/B_{\text{rms}} \approx 0.3$, as seen in Fig. 8 around $z \approx 650$.

We fit to the obtained velocity data (i) a power law $u \approx (1+z)^{-\beta}$ for the drag regime and (ii) an exponential $u \approx \exp(-\alpha z)$ for the

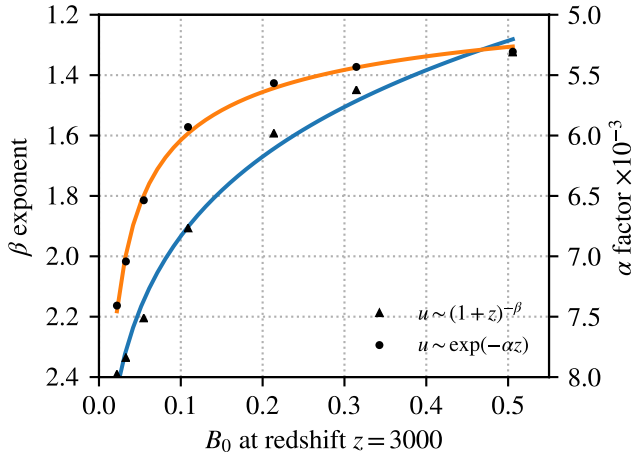


Figure 9. Parameters of the fitted curves describing the evolution of the velocity field u_{rms} in Fig. 8. We fitted a curve for the drag dominated regime with $u \approx (1+z)^{-\beta}$ (triangles), one for the transition regime with $u \approx \exp(-\alpha z)$ (circles). The data points were then fitted with a power-law to give an analytical representation of α and β , given in Eq. (40)

transition regime. This enables us to derive simple semi-analytical fit formulae plotted in Fig. 9 for the parameters α and β of the growing velocity field, as a function of B_0 .

$$\begin{aligned} \alpha &= (4.49 + 0.57 B_0^{-0.42}) \times 10^{-3} \\ \beta &= 4.97 - 4.0 B_0^{0.12} \end{aligned} \quad (40)$$

The coefficient α in the transition exponential fit is steeper for lower initial field strengths B_0 , visible in the upper (orange) curve in Fig. 9, while the drag fit power-law exponent β plotted as the lower (blue) curve, varies less.

The last phase is that of turbulent decay where both u_{rms} and B_{rms} decrease slowly at $z < 600$. This occurs for all simulation runs of the amplitude variation in a similar fashion, but with a greater overall decay for larger initial amplitude B_0 . In the next section we compare the magnetic energy dissipation rates to those expected from turbulence. Although the rate of decline of B_{rms} was faster in the transition era, the overall decline in the turbulent decay regime till its end (at $z = 100$ in the simulation) is comparable to the decline in the transition regime. However, the decline in the velocity field rms amplitude over the turbulent regime, by at most a few tens of a percent up to a factor of two, is much slower than its rapid rise by more than an order of magnitude in the two earlier regimes.

The redshift at which turbulence becomes important for the velocity field is illustrated in Fig. 10, where we plot the evolution of the magnetic Reynolds number $\text{Rm} = (v_A/L)/\tilde{\alpha}$, as a function of the initial magnetic field amplitude B_0 . For the fiducial case, $B_0 = 0.51$, the magnetic Reynolds number rises above unity only at redshift $z \lesssim 650$ which matches the epoch where turbulent decay sets in for the velocity field, see Fig. 8. For weaker fields, the transition to the turbulent regime occurs even later.

5.2.2 Dissipation rates with varying magnetic amplitude

We now investigate the difference in the magnetic dissipation and baryon heating rates as a function of magnetic amplitude with the aim of possibly placing constraints on primordial magnetic fields.

The magnetic energy density dissipation rate (per logarithmic redshift interval), normalized to the energy density of radiation $d(Q_B/\rho_\gamma)/d \ln z$ is plotted for varying B_0 in Fig. 11. Note that

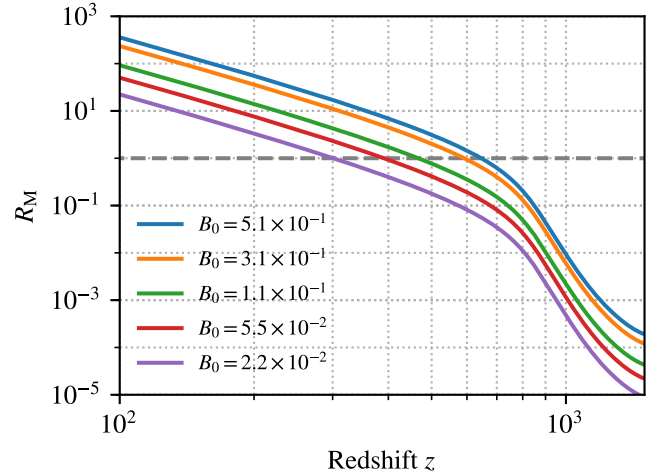


Figure 10. Magnetic Reynolds numbers as a function of redshift for simulation runs where B_0 is varied. The critical magnetic Reynolds number $\text{Rm} = 1$ is indicated with a grey dashed line. For different initial amplitudes the $\text{Rm} = 1$ redshift varies from $z_{\text{td}} \approx 650$ (fiducial $B_0 = 0.51$) to $z_{\text{td}} \approx 300$.

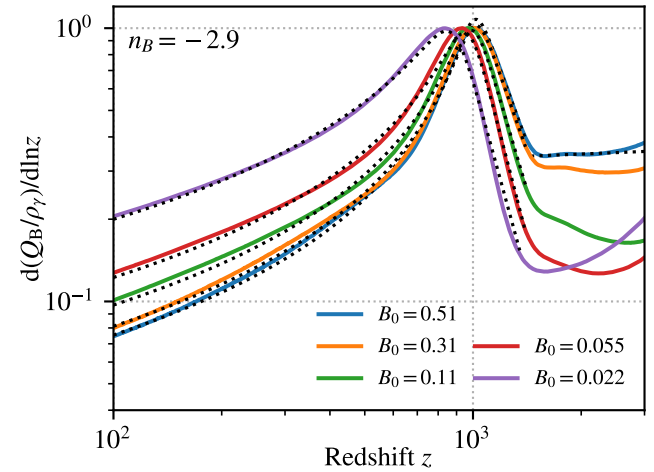


Figure 11. Comparison of the dissipation rate of the magnetic energy density with varying amplitude of the initial magnetic field B_0 . All curves were normalized to their peak amplitude. The $z \gtrsim 1500$ drag-dominated range is affected by numerical convergence issues for the lower amplitudes. Black dotted curves are fits (Eqs. 43 & 45) for turbulent and transition regimes.

in this plot the curves have all been normalized to their peak value, $[d(Q_B/\rho_\gamma)/d \ln z]_{\text{peak}}$. The normalization in physical units as a function of B_0 is given separately in Fig. 13. We find that there is a dependence on B_0 of the redshift at which the magnetic energy density dissipation peaks, particularly for the weaker fields. The peak redshift varies from $z \approx 1020 - 820$ over the range of magnetic field amplitudes $B_0 = 0.51 - 0.022$ while exhibiting a non-linear $z_{\text{peak}} \leftrightarrow B_0$ relation.

Another trend that was observed by varying the field strength amplitude was that the height of the peak compared to the magnetic energy dissipation rate values at $z \approx 1500$ in Fig. 13 is a monotonic function of B_0 . We find an increase of $dQ_B/d \ln z$ by a factor of ≈ 3 for $B_0 = 0.51$ (blue line) and an increase by a factor of ≈ 8 for the run with lowest amplitude with $B_0 = 2.2 \times 10^{-2}$ (red line). The shape of $dQ_B/d \ln z$ between $z = 3000$ and $z = 1500$ is less robust and also more susceptible to numerical issues so we ignore

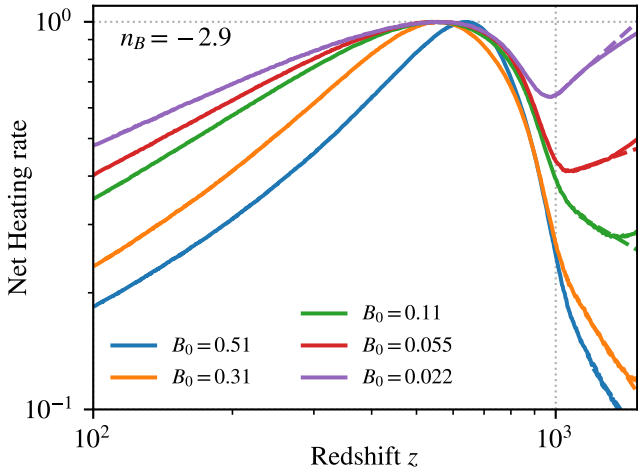


Figure 12. Net heating rates for different initial magnetic field strengths B_0 . For the high B_0 runs the peak of the net heating is well-pronounced. The low amplitude runs are dominated by hyperviscosity at high- z , so dashed lines were plotted to show the physical decline of net heating for earlier times.

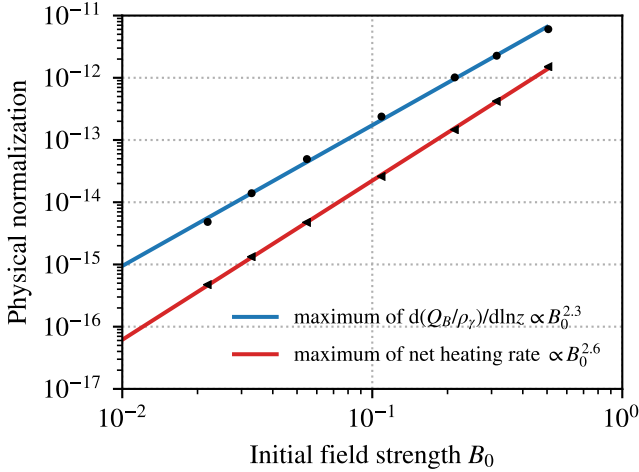


Figure 13. Physical normalization of the magnetic dissipation rate $dQ_B/d \ln z$ (Fig. 11) at its peak (blue line) and the net heating rate (Fig. 12) at its peak (red line), for different initial field strengths B_0 .

those values, since we do not extract any physical properties from the simulation during this period. For the $B_0 = 0.51$ the high- z behaviour can be described by a power-law

$$\left. \frac{d(Q_B/\rho_\gamma)}{d \ln z} \right|_{\text{drag}} = 0.23 \times (1+z)^{0.054}. \quad (41)$$

For the lower amplitudes the numerical noise is too strong at those early redshift, so we do not infer anything from the high- z behaviour. For the magnetic dissipation rate, the peak position does not coincide with $\text{Rm} \approx 1$, but rather with the epoch at or just before when magnetic and kinetic energy densities reach closest to equipartition (see Fig. 8). The real importance of turbulence can only be appreciated when considering the net heating rates (see Fig. 12 and discussion below), which show that for a large redshift range the PMF evolution for small magnetic fields is only weakly turbulent. This leads to a net heating rate with a very broad maximum, in contrast to previous analyses.

The net heating rate is computed by subtracting the dissipation

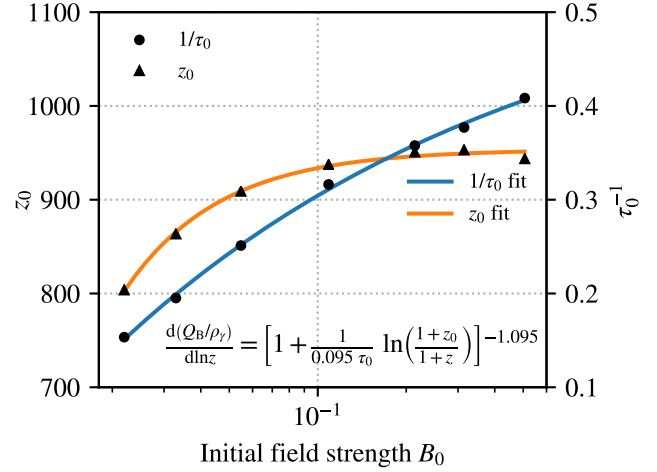


Figure 14. Fitting parameters for the semi-analytic formula used to describe the magnetic dissipation rates (Fig. 11) in the turbulent decay regime for different B_0 . The redshift parameter z_0 saturates towards $z \sim 950$ whereas the parameter $1/\tau_0$ increases for larger B_0 .

due to drag, which can be calculated as $2(\tilde{\alpha} + 1/2)E_{\text{kin}}$, from the total energy dissipation rate $dE_{\text{tot}}/d \ln z$. In Fig. 7 we had displayed the rates of E_{mag} , E_K , E_{tot} , drag dissipation rate and the net heating rate for our fiducial case, $\nu_3 = 2.5 \times 10^{-16}$, $B_0 = 0.51$. We now show the net heating rates $[dE_{\text{tot}}/d \ln z - 2(\tilde{\alpha} + 1/2)E_{\text{kin}}]/\rho_\gamma$ for the simulation runs with varying magnetic amplitudes in Fig. 12. The net heating rate peaks at similar redshifts $z \sim 550 - 650$, with most of the small shift in epoch occurring between $B_0=0.51$ and 0.31 . It rises to a peak over a roughly similar redshift range towards the end of the transition regime, once the drag dissipation has become negligibly small, and the peak epoch does not strongly depend on varying B_0 . The peak epoch of the net heating is significantly later (~ 0.5 Myr) compared to the peak of magnetic dissipation, for all B_0 values, as already mentioned above, due to the time taken to develop sufficiently turbulent velocity fields. Another new result from these simulations is that net heating generally does not peak sharply but over a broad range of redshifts, increasingly so for weaker initial amplitudes B_0 . The strongest amplitude case $B_0 = 0.51$ (blue) lowest curve in Fig. 12) has the most pronounced peak at $z \approx 650$ in the heating. For the lower B_0 runs the peak is very broad and almost constant over a considerable range of redshifts $z \sim 500 - 700$.

In Fig. 13 we show the physical normalizations of the amplitude of the peak of $dQ_B/d \ln z$ (blue line), as well as the maximum value of the net heating rate (red line) as a function of the initial magnetic field strength B_0 . We find that the magnetic energy dissipation rate has the following dependence of the initial magnetic field in our simulations:

$$\left. \frac{d(Q_B/\rho_\gamma)}{d \ln z} \right|_{\text{peak}} = 3.17 \times 10^{-11} \times B_0^{2.26} \quad (42a)$$

$$\left. \frac{dQ_{\text{net heat}}}{d \ln z} \right|_{\text{peak}} = 8.04 \times 10^{-12} \times B_0^{2.55}. \quad (42b)$$

Since the magnetic energy dissipation rate is simply the logarithmic derivative of the magnetic energy density $\propto B^2$, we expect a scaling of $dQ_B/d \ln z \propto B_0^2$. The observed scaling of the amplitude in our runs is slightly steeper than quadratic.

5.2.3 Semi-analytic representation of magnetic dissipation

We also show fits to the turbulent and transition regime portions of the magnetic dissipation rates as a function of B_0 . For the low redshift turbulent decay dominated part, we fit an inverse logarithmic function of the form derived phenomenologically in Eq. (24), for the case of a near scale-invariant magnetic spectrum $n_B = -2.9 \Leftrightarrow m = 0.095$:

$$\left. \frac{d(Q_B/\rho_\gamma)}{d \ln z} \right|_{\text{turb}} = \left(1 + \frac{1}{(0.095)\tau_0} \ln \frac{1+z_0}{1+z} \right)^{-1.095}. \quad (43)$$

This fitting process for parameters τ_0 and z_0 was applied over a range of low redshifts $z \in [100, z_{\text{max}}]$, where z_{max} ranges from 500 to 900, for initial amplitude $B_0 = 0.51 - 0.022$. This fitting range was chosen to give better agreement in the lower redshift part of the turbulent regime. The resulting parameters for the semi-analytic magnetic energy dissipation rate are shown in Fig. 14. By applying a power-law fit to the obtained values we can give a description of the parameters z_0 and τ_0^{-1} as a function of the initial magnetic field strength B_0 :

$$\begin{aligned} z_0 &= 959 - 2.37 B_0^{-1.08} \\ \tau_0^{-1} &= 0.75 - 0.30 B_0^{0.17}. \end{aligned} \quad (44)$$

We should note that the fitted coefficients and exponents given above are somewhat sensitive to the chosen redshift range in which the fit is performed.

In the transition regime, on the high redshift side of the maximum rate of change of the magnetic energy density, we fitted a power-law of the form:

$$\left. \frac{d(Q_B/\rho_\gamma)}{d \ln z} \right|_{\text{trans}} = A \times (1+z)^{-\beta}, \quad (45)$$

where $\beta \in [3.6, 5.0]$. The two separate fits over the turbulent and transition regimes were co-added with a cubic exponent and over-plotted as black dotted lines in Fig. 11,

$$\left. \frac{d(Q_B/\rho_\gamma)}{d \ln z} \right|_{\text{drag}} = A \times (1+z)^\gamma. \quad (46)$$

With $A = 0.23$ and $\gamma = 0.054$. For $B_0 = 0.51$. The simulation of the lower amplitudes B_0 have not fully equilibrated at high- z and the behaviour of $dQ_B/d \ln z$ is dominated by numerical effects, resulting in slopes γ that show non-monotonic behaviour as a function of B_0 , so we only fit for the run with highest B_0 .

5.3 Dependence on spectral index

Since we set up the magnetic field power spectrum as an initial condition, we have the freedom to vary its spectral shape. A scale-invariant magnetic power spectrum $P_M \propto k^{-0.9}$ is expected from models of inflationary magnetogenesis (Subramanian 2016). We also know that $P_M \propto k^4$ is an initial power spectrum that represents a magnetic field generated in a causal process, like a first-order phase transition (Durrer & Caprini 2003). Probing PMF evolution for different magnetic spectra thus has the potential to constrain and discern among different models of magnetogenesis. In the following subsections we describe the trend of physical results from simulation runs with varying spectral indices.

5.3.1 Evolution of magnetic and kinetic field amplitudes

In Fig. 15 we show the redshift evolution of the magnetic field B_{rms} in the upper panel and the velocity field u_{rms} in the lower panel.

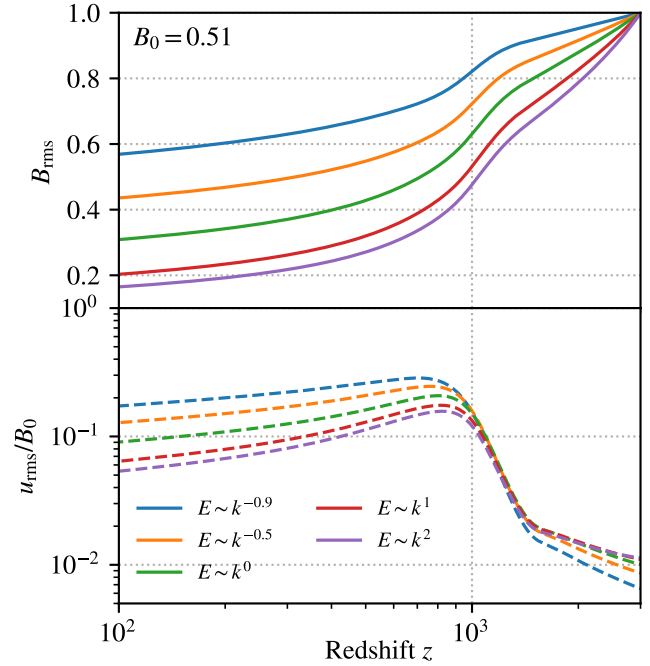


Figure 15. Evolution of the rms amplitudes with different initial spectra. The solid lines give the magnetic field strength, the dashed lines are the rms velocity in the simulation. For the steep spectra the same initial integral scale was used.

The different curves correspond to (from top to bottom in the upper panel) a near scale-invariant spectrum $P_M \propto k^{-0.9}$ (blue), two flatter spectra $P_M \propto k^{-0.5}$ (orange), $P_M \propto k^0$ (green) and two steep spectra with $P_M \propto k^1$, $P_M \propto k^2$ which are plotted as red and purple lines, respectively. The curves for B_{rms} and u_{rms} were normalized at $z = 3000$, when the ring-in phase of the velocity field died down. It should be kept in mind that the relative evolution between $z = 3000$ and the starting redshift of the simulation depends on the spectral index.

For the magnetic field strength B_{rms} there is a clearer difference in its evolution as a function of its spectrum. The scale-invariant case shows the least decay: its B_{rms} value at $z = 100$ is 60% of the initial value at $z = 3000$, with a greater fraction of the decay happening during the later phases $z < 1000$. On the other hand, the steepest spectrum $P_M \propto k^4$ decays by almost an order of magnitude during the simulation, with more than half the decline occurring prior to $z = 1000$. In general, there seems to be a clear distinction between the B_{rms} evolutionary shape for the scale-invariant case and the steeply evolving most blue spectra. Steepening the spectral index among the blue spectra (k^1, k^2) only slightly changes their magnetic amplitude evolution and they exhibit a very similar decay shape.

For the velocity field there is no strong dependence on the spectral index of the initial magnetic field at high- z in the drag and transition regimes. All curves show a similar slope and amplitude except the scale-invariant fiducial case where velocities grow slightly faster. Only at lower redshifts, below $z < 800$ and in the turbulent regime do the differences become apparent. The larger the initial spectral index n is, the closer one gets to equipartition, defined in our units as equality of u_{rms} and B_{rms} . Also, the runs with steeper initial spectra show more pronounced turbulent decay of velocities.

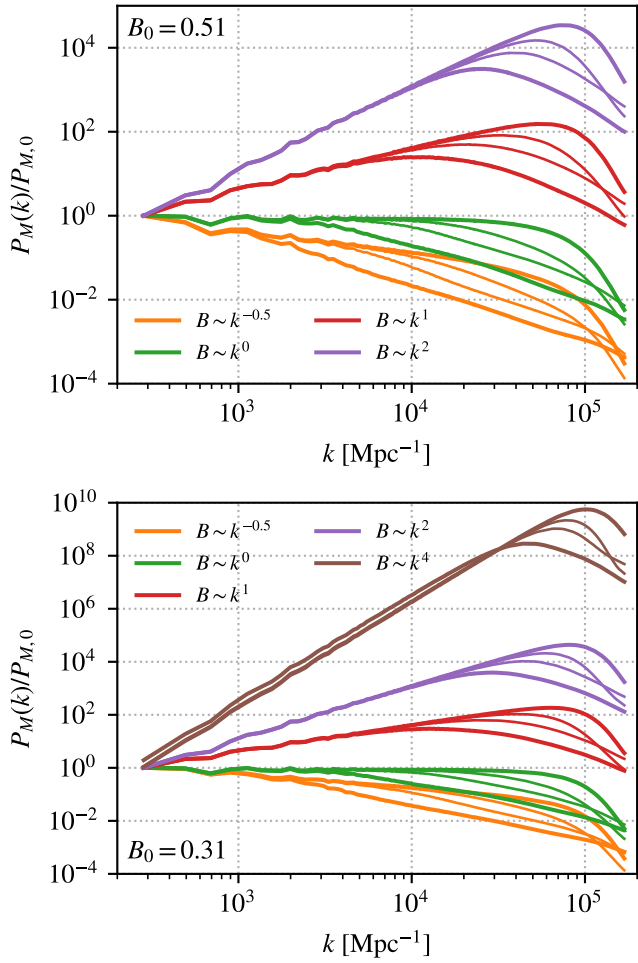


Figure 16. Evolution of the magnetic power spectra with different spectral index n , at four redshifts $z = 3000, 1200, 900$ & 400 , decreasing from top to bottom in each panel. The upper panel is for $B_{z=3000} = 0.51$ while the lower shows the curves for $B_{z=3000} = 0.31$. For $B_{z=3000} = 0.31$, a causal initial spectrum, $P_M \propto k^4$, is also simulated and shown.

5.3.2 Magnetic power spectra

We show the magnetic power spectra $P_M(k)/P_M(0)$ in Fig. 16 evolving through the same redshifts $z = 3000, 1200, 900$ & 400 as in Fig. 6 but now for a range of initial spectral indices. These spectra can be contrasted with the evolving spectra already presented for our fiducial case $B_0 = 0.51, n = -0.9$ in Fig. 6. We observe that for $B_0 = 0.51$ (upper panel of Fig. 16), the spectrum with $P_M \propto k^{-0.5}$ shows an evolution of the spectrum into a turbulent power-law over virtually all its k -modes. However, this is not the case for steeper spectral indices. For the $P_M \propto k^0$ case, the lowest wavenumber at which the initial spectrum has evolved into a turbulent Kolmogorov-like spectrum $P_M \propto k^{-5/3}$ is $k \approx 3.0 \times 10^3 (h/0.7) \text{ Mpc}^{-1}$. The power spectrum case of $P_M \propto k^1$, the reddest spectrum for which an integral scale k_I can be defined, displays $k_I \approx 3.8 \times 10^4 (h/0.7) \text{ Mpc}^{-1}$ at $z = 400$. For the $P_M \propto k^2$ the integral scale at $z = 400$ shifts to wavenumber $k_I \approx 4.8 \times 10^4 (h/0.7) \text{ Mpc}^{-1}$. All the integral and peak scales for bluer spectra shown in Fig. 16 are presented in Table 1.

In Fig. 16 (lower panel) we show the magnetic power spectra for the runs with a lower initial magnetic field strength of $B_0 = 0.31$, where the steepest case of an initial causally-generated

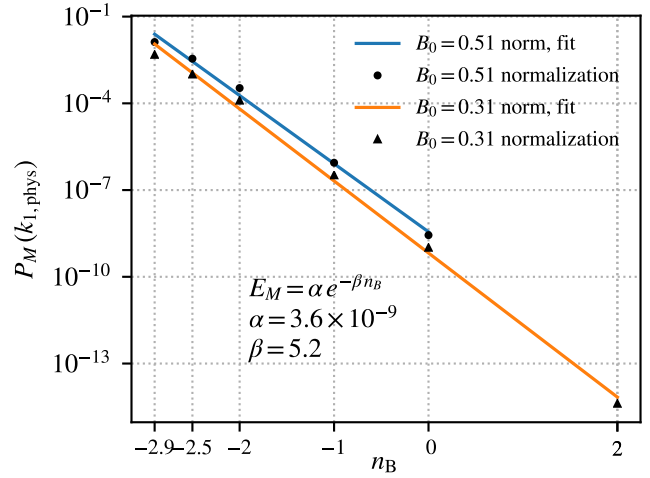


Figure 17. Relative normalization of the magnetic power spectra (shown in Fig. 16) at $k_{1,\text{phys}} = 280 (h/0.7) \text{ Mpc}^{-1}$ as a function of spectral index $n_B = n - 2$

Magnetic spectrum	integral scale k_I	peak scale
$B_0 = 0.51$		
$n = 1$	3.8×10^4	9.0×10^3
$n = 2$	4.8×10^4	2.4×10^4
$B_0 = 0.31$		
$n = 1$	4.0×10^4	1.2×10^4
$n = 2$	5.1×10^4	2.8×10^4
$n = 4$	6.4×10^4	4.6×10^4

Table 1. The integral and peak scale in physical units of $(h/0.7) \text{ Mpc}^{-1}$, for the more blue magnetic spectra, measured at $z = 400$ (spectra shown in Fig. 16)

power spectrum, $P_M \propto k^4$, is also presented. We observe that this case too develops a turbulent high- k tail for $k > k_I$ with $k_I \approx 6.4 \times 10^4 (h/0.7) \text{ Mpc}^{-1}$. The evolution of power spectra presented in Fig. 16 clearly demonstrate the establishment of a turbulent power-law over time, whose k -range is largest for scale-invariant spectra $k^{-0.9}$ and progressively restricted only to higher k -scales as the spectra become more blue to k^2 and k^4 . The blue spectrum simulation runs also exhibit the start of an inverse transfer effect for decaying non-helical turbulence. Reppin & Banerjee (2017) have shown that this can occur for steep spectra if Reynolds numbers are large enough and the integral scale k_I is peaked at sufficiently large k , which is the case here (also cf. Brandenburg et al. 2015).

The normalization of magnetic power spectra has been set by relating its integral to the chosen B_0 . The relative normalization of the magnetic power spectra as a function of spectral index $n_B = n - 2$ is shown in Fig. 17. The normalization is computed at the first binned wave vector value of $k_1 = 1.29$ which corresponds to $k_{1,\text{phys}} = 280 (h/0.7) \text{ Mpc}^{-1}$. The dependence of this normalization on the spectral index n_B follows an exponential form and Fig. 17 also gives a fit.

5.3.3 Dissipation rates and net heating rate

We now examine the changes in the magnetic energy dissipation rate and the net heating rate for the simulation runs with varying

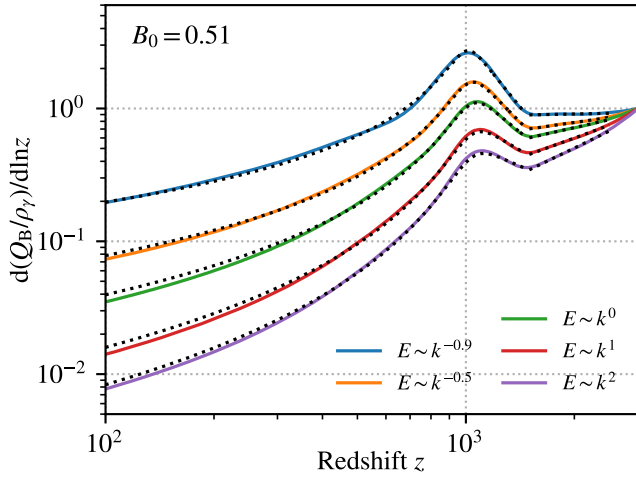


Figure 18. Comparison of dissipation rate of magnetic energy density when varying the spectral index $P_M k \propto k^n$, with $n = n_B + 2$. The curves are normalized to the values at $z = 3000$. The spectral index varies from -0.9 to 4 from top curve to bottom. We show combined fits (dotted curves) to the magnetic energy dissipation rates for the drag regime at high- z (Eq. 52), for the turbulent regime (Eq. 48) and for the transition region (Eq. 49).

spectral indices. Fig. 18 depicts the rate of change of the magnetic energy density. Note that here we have normalized all curves to their initial value at $z = 3000$. The peak redshift is virtually independent of spectral index n , tending slightly to earlier epochs for bluer spectra. In the drag dominated regime $z > 1500$, the slope of the energy dissipation rate becomes monotonically steeper with increasing n . This has the effect that the magnetic dissipation rate only rises above its initial value for spectra redder than $P_M \propto k^0$. In the turbulent regime, the dissipation rates all decline monotonically, by over a factor of 3 for the near scale-invariant spectrum and by around an order of magnitude for the bluest spectrum. We fit to each of these three regimes as described in the next subsection.

The net heating rate due to magnetic fields for different initial spectral indices $n = -0.9, -0.5, 0, 1$ & 2 is displayed in Fig. 19. Two different magnetic field amplitudes $B_0 = 0.51$ and 0.31 (including the additional spectral case of $n = 4$) are shown in the upper and lower panels respectively. The epoch of peak net heating shows a striking shift to higher redshifts as the spectral index varies from $n = -0.9$ to 2 or 4 . There is a clear distinction between the scale-invariant case $n = -0.9$, which peaks at a redshift $z \approx 650$, and the net heating for steeper initial spectra, which peak at earlier epochs up to $z \approx 925$. Thus magnetic spectral variation alone can delay the epoch of peak net heating by ~ 0.4 Myr. This effect is even more pronounced as B_0 is reduced from 0.51 to 0.31 , as expected from the amplitude variation of net heating described earlier in Fig. 12.

Overall, we discern two clear trends for the shape and position of the net heating rate as a function of magnetic field parameters: from earlier, as the field strength grows stronger, the net heating maximum is more sharply peaked in time. The second trend we see here is that as the magnetic spectral index is lowered (to near scale-invariant), the net heating peak is delayed by a greater time interval of up to 0.5 Myr after the epoch of recombination. To compare, this time-lag is greater than the age of the Universe at recombination.

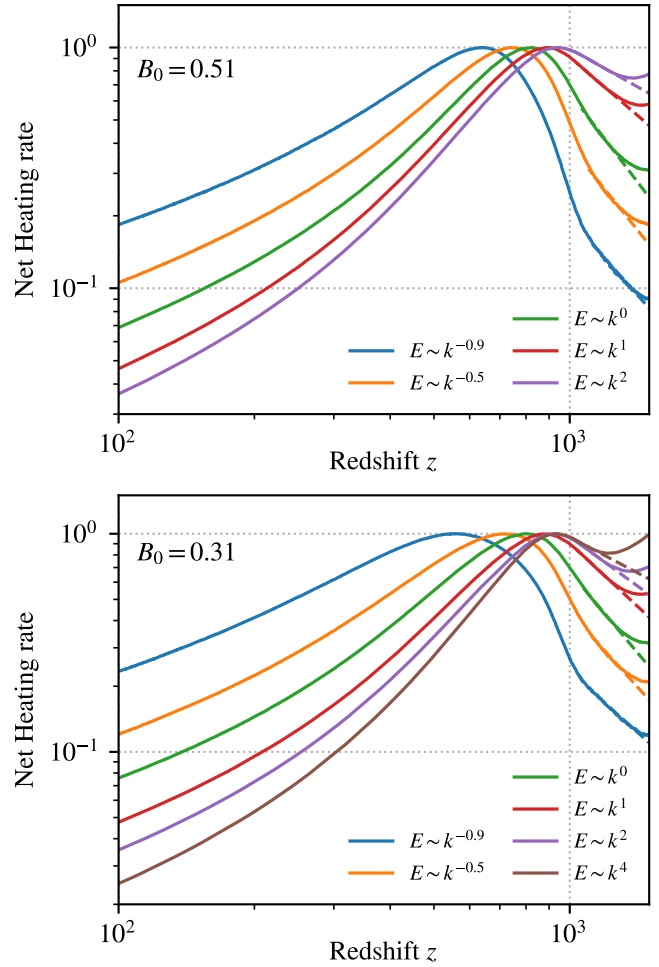


Figure 19. Net heating rate for different spectral indices n and two values of $B_0 = 0.51$ and 0.31 . The physical normalizations for both cases are presented in Fig. 20. The dashed lines show an extrapolation of the rates avoiding the numerical issues which dominate at large z and cause an unphysical rise, especially of the bluer spectra.

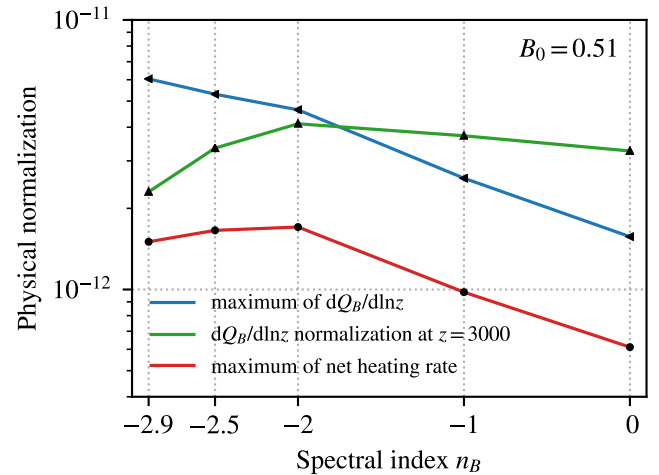


Figure 20. Physical normalization of the peak values (blue) and initial ($z = 3000$) values (green) of the magnetic energy density dissipation rate from Fig. 18 as well as the net heating rate peak values (red) from Fig. 19, all as a function of spectral index n_B where $n_B = n - 2$.

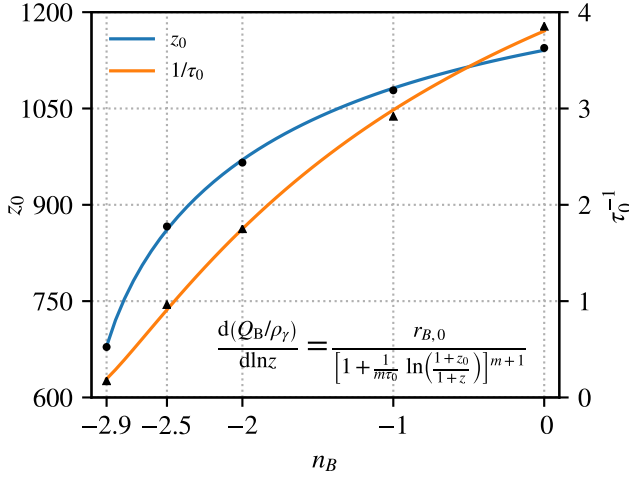


Figure 21. Fitting parameters for the magnetic energy density dissipation rate with varying spectral index in Fig. 18 in the turbulent decay regime. The rates were fitted using Eq. (47) over the range $z \in [100, 900]$. A power-law was then fitted to give a functional form of z_0 and τ_0^{-1} in Eq. (48).

5.3.4 Semi-analytic representation of the PMF losses

In this section, we construct a semi-analytic representation of the total magnetic energy density dissipation rates. We provide separate fits for the turbulent, transition and drag-dominated regimes which we then combine together to plot as the black dotted curves in Fig 18.

In the turbulent regime, following the phenomenological derivation presented in Sect. (3.3), we use the functional form

$$\left. \frac{d(Q_B/\rho_\gamma)}{d \ln z} \right|_{\text{turb}} \approx \frac{r_{B,0}}{\left[1 + \frac{1}{m\tau_0} \ln\left(\frac{1+z_0}{1+z}\right) \right]^{m+1}}, \quad (47)$$

with free parameters τ_0 and z_0 as a starting point. We recall that $m = 2(n_B + 3)/(n_B + 5) = 2(n + 1)/(n + 3)$. The late-time behavior of the curves shown in Fig. 18 can then be represented by

$$r_{B,0} \approx 1 \quad (48a)$$

$$z_0 = 532 + 549 m^{0.56} \quad (48b)$$

$$\tau_0^{-1} = 0.07 + 2.91 m^{1.36}. \quad (48c)$$

Since the denominator in Eq. (47) vanishes at $z_{\text{lim}} \approx z_0 e^{m\tau_0}$, Eq. (47) is only valid at $z < z_{\text{lim}}$, where $z_{\text{lim}} \in [1190; 1560]$, and the turbulent regime lies well within this range. The power-law fits for z_0 and τ_0^{-1} are plotted in Fig 21 as a function of spectral index n_B .

Next, the transition regime between drag-dominated ($z \gtrsim 1500$) and pure turbulent-decay ($z \lesssim 800$), can be represented using a simple power-law scaling:

$$\left. \frac{d(Q_B/\rho_\gamma)}{d \ln z} \right|_{\text{trans}} \approx A \left[\frac{1300}{1+z} \right]^\beta. \quad (49)$$

To represent the rising dissipation rates from the drag regime to their peak values in Fig. 18, we find

$$A \approx 1.59 - 1.04 m^{0.64} \quad (50a)$$

$$\beta = 3.51 - 1.94 m \quad (50b)$$

to work very well. For the transition regime the power-law was fitted in a redshift range of $z \in [1500, 1200]$.

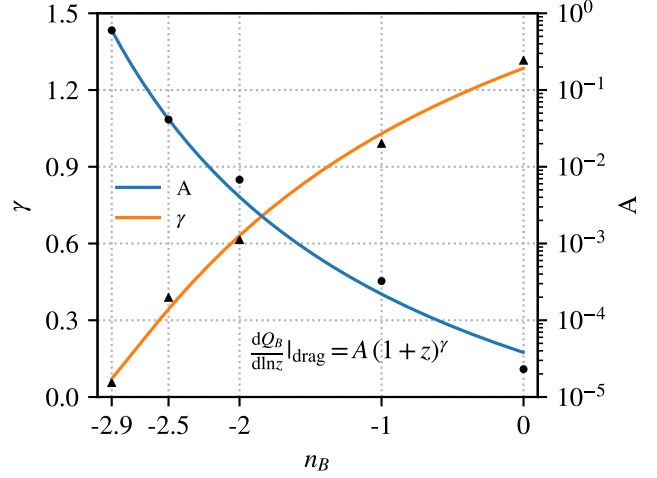


Figure 22. Fitting parameters for the high- z drag-dominated magnetic energy dissipation rate in Fig. 18, as a function of spectral index. The fit equations for the power-law parameters A and γ are given in Eq. (52)

To approximate the evolution at the high redshift drag-dominated regime, we fit a power-law of the following form

$$\left. \frac{d(Q_B/\rho_\gamma)}{d \ln z} \right|_{\text{drag}} = A (1+z)^\gamma \quad (51)$$

to the magnetic energy dissipation rate in Fig. 18 for $z \in [1500, 2500]$. This gives the observed slopes shown in Table 2. If we parameterize the slope β and the amplitude A as a function of the initial spectral index m we get:

$$A = 1.38 e^{-8.75 m} \quad (52a)$$

$$\gamma = 0.015 + 1.01 m^{1.23}. \quad (52b)$$

We normalize the curves at $z = 3000$. Fig. 22 shows the parameterization of the fits to the high redshift range in Fig. 18.

In the pre-recombination drag dominated regime, the theoretical prediction derived in Sect. 3.2.1 for the magnetic energy density dissipation rate $dQ_B/d \ln z \propto \rho_\gamma(z) (1+z)^{5(n_B+3)/2(n_B+5)}$ is qualitatively comparable to the trend of the fitted slopes γ as a function of spectral index - see Table 2. We note that our numerical simulations do not explicitly match the predicted high- z scaling (cf. Eq. 13) because of numerical effects (discussed in Appendix A) and also due to our assumption of matter-domination (see discussion in Sect. 3.2.2).

For a combined fit for the dissipation rates for each spectral index over all three regimes, we found that a cubic exponent gives a good approximation for combining the turbulent and transition fits at lower redshifts,

$$\frac{d(Q_B/\rho_\gamma)}{d \ln z} \approx \begin{cases} \left[\left. \frac{d(Q_B/\rho_\gamma)}{d \ln z} \right|_{\text{turb}} + \left. \frac{d(Q_B/\rho_\gamma)}{d \ln z} \right|_{\text{trans}} \right]^{-1/3} & z \lesssim z_{\text{lim}} \\ \left. \frac{d(Q_B/\rho_\gamma)}{d \ln z} \right|_{\text{trans}} & z \lesssim 1300 \\ \max \left(\left. \frac{d(Q_B/\rho_\gamma)}{d \ln z} \right|_{\text{trans}}, \left. \frac{d(Q_B/\rho_\gamma)}{d \ln z} \right|_{\text{drag}} \right) & z \gtrsim 1300. \end{cases} \quad (53)$$

With this we obtain the fit functions over plotted as the dotted black curves shown in Fig. 18.

n_B	observed slope	fitted γ	predicted slope
-2.9	0.05	0.07	0.12
-2.5	0.39	0.34	0.50
-2.0	0.61	0.63	0.83
-1.0	0.99	1.03	1.25
0.0	1.31	1.28	1.50

Table 2. Comparison of the observed (Fig. 18) and fitted slope γ (Eq. 52) versus the predicted slope $5(n_B + 3)/2(n_B + 5)$ for the dissipation rate of magnetic energy density in the high redshift drag-dominated regime.

6 DISCUSSION

We discuss below some of the caveats of our computations. There are related to i) resolution and numerical viscosity, ii) baryon density perturbations and shocks for $B_0 > 10^{-2}$ nG, iii) self-gravity and photon perturbations, iv) changes induced to the drag coefficient.

Let us start with resolution issues. Our technique of solving the MHD equations on a grid means that we are limited to about three orders of magnitude in dynamic range in k -space with our resolution of $N = 1536^3$. However, we can still adequately trace the evolution of the power spectra as well as the individual kinetic and magnetic energy densities. Going to higher resolution will greatly increase the computational costs but it will also increase the range in k -space that can be resolved. This would allow us to separate the drag-dominated damping scale more cleanly from the Nyquist scale, hence reducing numerical artifacts.

At the highest redshifts ($z > 3000$) of our simulation, the evolution of the energy dissipation rates is still affected by numerical viscosity leading to a ring-in phase of the velocity field and a slight underestimation of the magnetic dissipation rate (since part of the energy branches into numerical heating). However, we performed several tests in this regime, strongly reducing the numerical viscosity. This showed that the PMF evolution is well understood and by the transition epoch, numerical viscosity no longer significantly affects our heating rates. Thus, we are able to reliably deduce the net heating rates that go into the plasma from the decay of the magnetic energy density at $z \approx 3000$ to $z \approx 100$.

In our simulation setup we are restricted to sub-sonic Alfvén velocities. This limits us to $B_{0,\text{phys}} \lesssim 4 \times 10^{-2}$ nG for physical values of the magnetic field in our runs. While still physically interesting and instructive, this level of PMFs is more than one order of magnitude below the level currently constrained using CMB data, $B_{0,\text{phys}} \sim 1$ nG (Planck Collaboration et al. 2016). In this regime of stronger magnetic fields, one has to consider significant perturbations in the plasma as well as shocks, which we have ignored in our case of low Mach numbers. We expect this to increase the heating efficiency of the PMFs, with kinetic energy being converted into heat more rapidly. We could expect that the transient regime becomes shorter and the net heating might also evolve accordingly. This will have further implications for structure formation, so a simulation that takes such effects into account will be needed for the future treatment of heating due to stronger magnetic fields.

Stronger magnetic fields could also source significant additional baryon density perturbations which can grow after recombination. While we have ignored these in the present simulation involving relatively weak magnetic fields, they could play a role with stronger magnetic fields: altering the Jeans scale for structure formation (Subramanian & Barrow 1998; Sethi & Subramanian 2005) as well as potentially constraining the PMF via contribution to the small-scale matter power spectrum and further effects

(Shaw & Lewis 2012; Jedamzik & Abel 2013; Pandey et al. 2015; Jedamzik & Saveliev 2018).

Similarly, we neglected self-gravity and photon perturbations in our simulation. In the drag-dominated regime, small-scale photon perturbations will be created. Part of these perturbations could affect the subsequent evolution of the plasma in the turbulent phase. They will also become visible as ultra-small scale CMB anisotropies, well below the photon diffusion scale $k \gtrsim 0.2 \text{ Mpc}^{-1}$. At late stages, we also expect the growth of dark matter halos to influence the dynamics of the fluid flow. This will be particularly important at $z \lesssim 100 - 200$, when ambipolar diffusion should also become relevant (Jedamzik et al. 1998). In refined treatments of the problem, these effects should be considered carefully.

In our simulations, we used the pre-computed standard recombination history obtained with CosmoRec (Chluba & Thomas 2011) to determine the drag coefficient. However, significant heating by PMFs can directly affect the recombination history (e.g., Sethi & Subramanian 2005; Chluba et al. 2015), which in turn would modify the drag terms. We expect these effects to only become noticeable for higher PMF strength ($B_0 \approx 1$ nG), when shocks also have to be considered. Therefore, the heating rates obtained here should be relatively robust with respect to this aspect.

Finally, in our simulations we only considered non-helical magnetic fields. However, PMFs may have been generated with substantial helicity (Vachaspati 2001) which would significantly alter their subsequent evolution (Banerjee & Jedamzik 2004) as well as produce distinct cosmological signatures (Pogosian et al. 2002; Planck Collaboration et al. 2016; Ballardini et al. 2015; Long & Vachaspati 2015). The influence of magnetic helicity conservation as well as inverse cascade on the evolution and decay of PMFs in this case would be interesting to explore and is left for future work.

7 CONCLUSIONS

We performed 3D numerical simulations of PMFs along with baryon velocity fluctuations across the cosmological recombination era. Photon drag was included using the standard recombination history obtained with CosmoRec and the MHD equations were solved in an expanding medium. Our simulations allow us to trace the flow of energy from the magnetic field, through the baryon velocity field to heating via turbulent decay and dissipation. We are able to describe the net heating rates smoothly across the epoch of recombination. This has enabled a clean separation of real heating, which will lead to an increase of the matter temperature, from drag-dominated magnetic energy losses to the CMB photon field, which only lead to secondary CMB temperature perturbations and spectral distortions.

We supported our computations with analytic estimates and provide several useful expressions to represent our numerical results. We find that at redshifts below $z \lesssim 500$, in the regime of well-developed turbulent decay, our new analytic approximation eq. (24) with an additional $1/m$ factor gives a good fit.

Three main evolutionary stages for magnetic heating are observed (Fig. 7): i) an initial phase that is dominated by photon drag ($z \gtrsim 1500$), ii) an intermediate transition period around cosmological recombination, when the photon drag force drops rapidly, and iii) the final fully turbulent MHD phase ($z \lesssim 600$). Only in the later part of the transition and the turbulent phase do we find significant heating of the medium, a result that is important when deriving and interpreting constraints on PMFs from CMB measurements.

Our computations show that the growth of baryon velocity

fluctuations is strongly suppressed at early times because of high photon drag, but builds up during the intermediate transition phase (Fig. 8). After recombination, a velocity saturation state approaching equipartition between magnetic and kinetic energy is reached, after which the plasma dissipates energy in a turbulent cascade. In previous treatments, the build-up of the velocity field and its turbulent decay were assumed to proceed instantaneously or in a prescribed fashion at recombination ($z \approx 1100$). Our simulations reveal a substantial delay for the onset of turbulence until redshift $z \approx 600 - 900$ (this depends on the amplitude and shape of the initial magnetic power spectrum). In the transition phase, the magnetic field decay continuously sources the baryon velocity field until a well developed turbulent state is reached, a process that causes a delay of up to 0.5 Myr.

We also find that the shapes of the net heating rates obtained are broader than previously estimated semi-analytically. For weaker magnetic fields, their peak broadens to extend to significantly lower redshifts ($z \lesssim 400$). In these cases, the fluid flow reaches turbulence more gradually with the magnetic Reynolds number exceeding unity only in the very late stages (Fig. 10). In contrast, steeper spectra ($n \sim 1 - 4$) produce an earlier peak in the net heating rates at $z_{\text{peak}} \approx 900$. The shape, epoch and width of the peak of the net heating rate are seen to depend significantly on the initial amplitude of the magnetic fields and their spectral index (Fig. 12 and Fig. 19). Our simulations further reveal that the peak magnetic energy density dissipation rate occurs once the drag coefficient has already dropped appreciably and the fluid approaches its maximum kinetic energy density growth rate (Fig. 8).

For the near scale-invariant case, almost the entire magnetic power spectrum (over two orders of magnitude) is reshaped to a turbulent power-law (Fig. 6) as a turbulent cascade removes and redistributes power. The turbulent slope obtained is $n \sim -1.4$, slightly shallower than Kolmogorov-type turbulence. On the other hand, we find that only the intermediate-scale wave modes $k > 1.0 \times 10^4 \text{ Mpc}^{-1}$ are reprocessed for spectra with $P_M \propto k^1$ and only the smallest scale modes $k > 5.0 \times 10^4 \text{ Mpc}^{-1}$ for the steepest spectrum $P_M \propto k^4$ (Fig. 16). The direct observation of the spectral transformation from an initial power-law with a cut-off to a spectrum in its transitional phase and then to a processed spectrum with a turbulent slope is a novel feature of our computations and a benefit of the full 3D treatment of the MHD equations.

To be able to achieve a more complete cosmological treatment, more physics at late times would need to be included: below a redshift of $z \lesssim 200$ effects like ambipolar diffusion could dominate and can contribute substantially to the evolution of the magnetic heating history at later epochs. Stronger magnetic fields along with compressible fluid phenomena would extend the scope of these simulations. A simultaneous treatment of density perturbations induced by PMFs would complement the evolution of heating and its cosmological effects. The results presented above represent a first step in simulating magnetic heating in cosmology and it would be interesting to extend them to describe magnetic signatures and constraints arising from the CMB, structure formation, 21-cm signals as well as the epoch of reionization.

ACKNOWLEDGMENTS

JC would like to cordially thank Ethan Vishniac and Geoff Vasil for useful discussions about magnetic turbulence. We would also like to thank Jacques Wagstaff for his contribution at an early stage of the project and Stefan Hackstein for comments. PT and JR are supported by the German Deutsche

Forschungsgemeinschaft (DFG), Sonderforschungsbereich (SFB) 676 section C9. JC is supported by the Royal Society as a Royal Society University Research Fellow at the University of Manchester, UK.

REFERENCES

- Ballardini M., Finelli F., Paoletti D., 2015, *JCAP*, 10, 031
 Banerjee R., Jedamzik K., 2004, *Phys.Rev.D*, 70, 123003
 Beck R., 2015, *The Astronomy and Astrophysics Review*, 24, 4
 Bernet M. L., Miniati F., Lilly S. J., Kronberg P. P., Dessauges-Zavadsky M., 2008, *Nature*, 454, 302
 Bonafede A., Feretti L., Murgia M., Govoni F., Giovannini G., Dallacasa D., Dolag K., Taylor G. B., 2010, *A&A*, 513, A30
 Bowman J. D., Rogers A. E. E., Monsalve R. A., Mozdzen T. J., Mahesh N., 2018, *Nature*, 555, 67
 Brandenburg A., Dobler W., 2010, *Pencil: Finite-difference Code for Compressible Hydrodynamic Flows*. *Astrophysics Source Code Library*
 Brandenburg A., Kahnishvili T., Tevzadze A. G., 2015, *Physical Review Letters*, 114, 075001
 Caprini C., Sorbo L., 2014, *JCAP*, 10, 056
 Chluba J., Khatri R., Sunyaev R. A., 2012, *MNRAS*, 425, 1129
 Chluba J., Paoletti D., Finelli F., Rubiño-Martín J. A., 2015, *MNRAS*, 451, 2244
 Chluba J., Sunyaev R. A., 2004, *A&A*, 424, 389
 Chluba J., Sunyaev R. A., 2009, *A&A*, 501, 29
 Chluba J., Sunyaev R. A., 2012, *MNRAS*, 419, 1294
 Chluba J., Thomas R. M., 2011, *MNRAS*, 412, 748
 Clarke T. E., Kronberg P. P., Böhringer H., 2001, *ApJL*, 547, L111
 Copi C. J., Ferrer F., Vachaspati T., Achúcarro A., 2008, *Phys. Rev. Lett.*, 101, 171302
 Dermer C. D., Cavadini M., Razzaque S., Finke J. D., Chiang J., Lott B., 2011, *ApJL*, 733, L21
 Dolag K., Kachelriess M., Ostapchenko S., Tomàs R., 2011, *ApJL*, 727, L4
 Durrer R., Caprini C., 2003, *JCAP*, 11, 10
 Durrer R., Neronov A., 2013, *The Astronomy and Astrophysics Review*, 21, 62
 Federrath C., Chabrier G., Schober J., Banerjee R., Klessen R. S., Schleicher D. R. G., 2011, *Physical Review Letters*, 107, 114504
 Feretti L., Giovannini G., Govoni F., Murgia M., 2012, *The Astronomy and Astrophysics Review*, 20, 54
 Fermi-LAT Collaboration, Biteau J., 2018, *ArXiv e-prints*
 Finelli F., Paci F., Paoletti D., 2008, *Phys.Rev.D*, 78, 023510
 Gasperini M., Giovannini M., Veneziano G., 1995, *Physical Review Letters*, 75, 3796
 Grasso D., Rubinstein H. R., 2001, *Phys.Rep.*, 348, 163
 Han J. L., 2017, *ARA&A*, 55, 111
 Hill J. C., Battaglia N., Chluba J., Ferraro S., Schaen E., Spergel D. N., 2015, *Physical Review Letters*, 115, 261301
 Jedamzik K., Abel T., 2013, *JCAP*, 10, 050
 Jedamzik K., Katalinić V., Olinto A. V., 1998, *Phys.Rev.D*, 57, 3264
 Jedamzik K., Katalinić V., Olinto A. V., 2000, *PRL*, 85, 700
 Jedamzik K., Saveliev A., 2018, *ArXiv:1804.06115*
 Kahnishvili T., Brandenburg A., Tevzadze A. G., Ratra B., 2010, *Phys.Rev.D*, 81, 123002
 Kaiser N., 1983, *MNRAS*, 202, 1169
 Kandus A., Kunze K. E., Tsagas C. G., 2011, *Phys.Rep.*, 505, 1
 Kim E.-J., Olinto A. V., Rosner R., 1996, *ApJ*, 468, 28
 Kronberg P. P., Bernet M. L., Miniati F., Lilly S. J., Short M. B., Higdon D. M., 2008, *ApJ*, 676, 70
 Kunze K. E., 2017, *Phys. Rev. D*, 96, 063526
 Kunze K. E., Komatsu E., 2014, *JCAP*, 1, 9
 Kunze K. E., Komatsu E., 2015, *JCAP*, 6, 027
 Long A. J., Vachaspati T., 2015, *JCAP*, 9, 065
 Ma C.-P., Bertschinger E., 1995, *ApJ*, 455, 7
 Mao S. A. et al., 2017, *Nature Astronomy*, 1, 621
 Martin J., Yokoyama J., 2008, *JCAP*, 1, 025

- Minoda T., Hasegawa K., Tashiro H., Ichiki K., Sugiyama N., 2017, Phys.Rev.D, 96, 123525
- Neronov A., Vovk I., 2010, Science, 328, 73
- Pandey K. L., Choudhury T. R., Sethi S. K., Ferrara A., 2015, MNRAS, 451, 1692
- Paoletti D., Finelli F., Paci F., 2009, MNRAS, 396, 523
- Peebles P. J. E., 1968, ApJ, 153, 1
- Planck Collaboration et al., 2016, A&A, 594, A19
- Pogosian L., Vachaspati T., Winitzki S., 2002, Phys.Rev.D, 65, 083502
- Pshirkov M. S., Tinyakov P. G., Urban F. R., 2016, Physical Review Letters, 116, 191302
- Ratra B., 1992, ApJL, 391, L1
- Refregier A., et al., 2000, Phys.Rev.D, 61, 123001
- Reppin J., Banerjee R., 2017, Phys.Rev.E, 96, 053105
- Schleicher D. R. G., Banerjee R., Klessen R. S., 2008a, Phys.Rev.D, 78, 083005
- Schleicher D. R. G., Banerjee R., Klessen R. S., 2009, ApJ, 692, 236
- Schleicher D. R. G., Galli D., Palla F., Camenzind M., Klessen R. S., Bartelmann M., Glover S. C. O., 2008b, A&A, 490, 521
- Sethi S. K., Subramanian K., 2005, MNRAS, 356, 778
- Sethi S. K., Subramanian K., 2009, JCAP, 11, 21
- Sharma R., Jagannathan S., Seshadri T. R., Subramanian K., 2017, Phys.Rev.D, 96, 083511
- Shaw J. R., Lewis A., 2010, Phys.Rev.D, 81, 043517
- Shaw J. R., Lewis A., 2012, Phys.Rev.D, 86, 043510
- Shiraishi M., Sekiguchi T., 2014, Phys.Rev.D, 90, 103002
- Shiraishi M., Tashiro H., Ichiki K., 2014, Phys.Rev.D, 89, 103522
- Sigl G., Olinto A. V., Jedamzik K., 1997, Phys.Rev.D, 55, 4582
- Subramanian K., 1998, MNRAS, 294, 718
- Subramanian K., 2006, Astronomische Nachrichten, 327, 403
- Subramanian K., 2010, Astronomische Nachrichten, 331, 110
- Subramanian K., 2016, Reports on Progress in Physics, 79, 076901
- Subramanian K., Barrow J. D., 1998, Phys.Rev.D, 58, 083502
- Sunyaev R. A., Chluba J., 2009, Astronomische Nachrichten, 330, 657
- Tavecchio F., Ghisellini G., Bonnoli G., Foschini L., 2011, MNRAS, 414, 3566
- Taylor A. M., Vovk I., Neronov A., 2011, A&A, 529, A144
- Trivedi P., Seshadri T. R., Subramanian K., 2012, Physical Review Letters, 108, 231301
- Trivedi P., Subramanian K., Seshadri T. R., 2014, Phys.Rev.D, 89, 043523
- Turner M. S., Widrow L. M., 1988, Phys.Rev.D, 37, 2743
- Vachaspati T., 1991, Physics Letters B, 265, 258
- Vachaspati T., 2001, Physical Review Letters, 87, 251302
- Wagstaff J. M., Banerjee R., 2015, Phys.Rev.D, 92, 123004
- Wasserman I., 1978, ApJ, 224, 337
- Weinberg S., 1971, ApJ, 168, 175
- Zeldovich Y. B., Kurt V. G., Syunyaev R. A., 1968, Zhurnal Eksperimentalnoi i Teoreticheskoi Fiziki, 55, 278
- Zucca A., Li Y., Pogosian L., 2017, Phys.Rev.D, 95, 063506

APPENDIX A: NUMERICAL VISCOSITY TESTS

To achieve a stable simulation over a wide range of redshifts, we tuned the hyperviscosity ν_3 in such a way that the bottleneck effect does not show up at late times ($z < 800$). Due to the drag being large at early times the simulation is stabilized and the magnetic field is frozen-in, whereas at late times hyperviscosity is needed in order to have a stable simulation run. In Fig. A1 we show the magnetic power spectra for $B_0 = 0.31$ at a redshift of $z = 750$ for different hyperviscosity parameters ν_3 ranging from $\nu_3 = 1 \times 10^{-17}$ to $\nu_3 = 5 \times 10^{-16}$. We chose a value of $\nu_3 = 2.5 \times 10^{-16}$ to get a power-law over a large range of k modes. Also, the highest value $\nu_3 = 5 \times 10^{-16}$ already shows an exponential cutoff at $k \approx k_{Ny}$, which causes the power spectrum not to be a smooth power-law. We wanted to produce as little dissipation as needed, so the highest value we tested in our runs turned out to be too large.

To ensure the results we obtain in our simulations do not depend on the viscosity parameter ν_3 in our setup, we ran multiple runs with varying

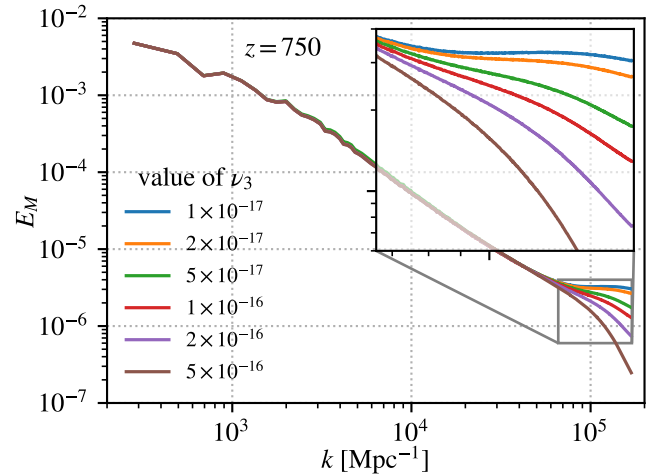


Figure A1. Comparison of magnetic power spectra for varying hyperviscosity ν_3 . Using a value $\nu_3 < 2 \times 10^{-16}$ gives excess power at high k . This is called the bottleneck effect which we avoid by choosing $\nu_3 = 2.5 \times 10^{-16}$

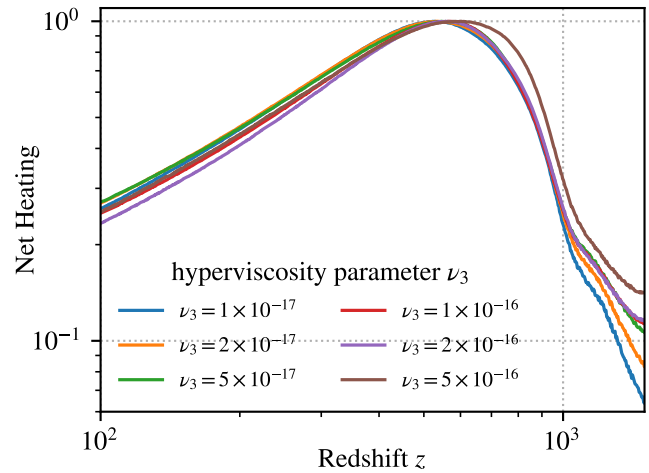


Figure A2. Dependence of the net heating rate for different ν_3 runs. The heating rate goes toward zero for low viscosities. We expect this behavior since the only dissipation at high- z should be from the drag. This curve is used to extrapolate the physical net heating rate for high- z drag-dominated regime.

runtime parameters for ν_3 . In Fig. A2 we plot the net heating rate for different ν_3 for the amplitude $B_0 = 0.31$. At high redshift $z > 1000$ we see that there is some dependence of low values of the heating rate on the numerical viscosity. We expect the net heating rate to be very low at high z since we are in the drag dominated regime and all dissipation should be due to the drag force.

APPENDIX B: RESOLUTION STUDY

We demonstrate the convergence of our simulation with respect to different choices of numerical resolution. For this resolution convergence test the setup with $B_0 = 0.31$, $\nu_3 = 2.5 \times 10^{-16}$ and a near scale-invariant initial magnetic power spectrum with four resolutions $N = 512^3$, $N = 768^3$, $N = 1024^3$, & $N = 1536^3$ were run. In Fig. B1 we show the redshift evolution of velocity & magnetic field strength u_{rms} & B_{rms} at late times, between $z = 3000$ and $z = 100$. We see that the runs converge nicely, with only the

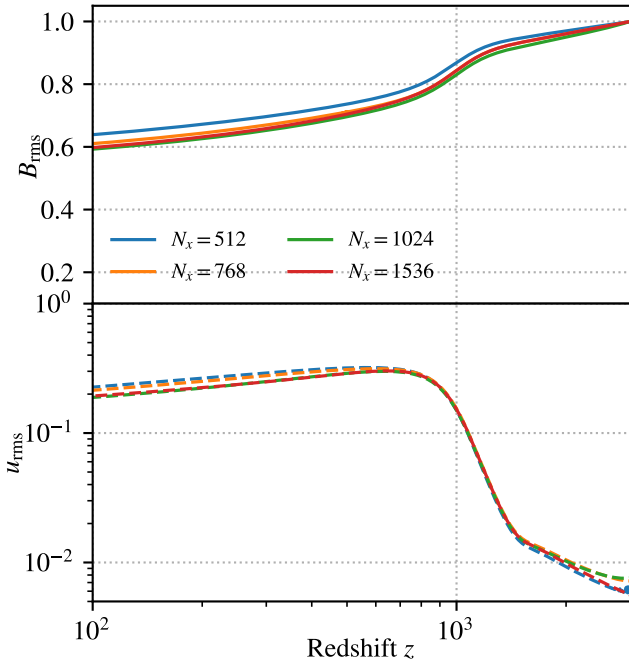


Figure B1. Redshift evolution of the magnetic field strength B_{rms} and the velocity field u_{rms} as a function of the resolution. The high resolution runs converge very well and even for the low resolution there is agreement on the qualitative behaviour.

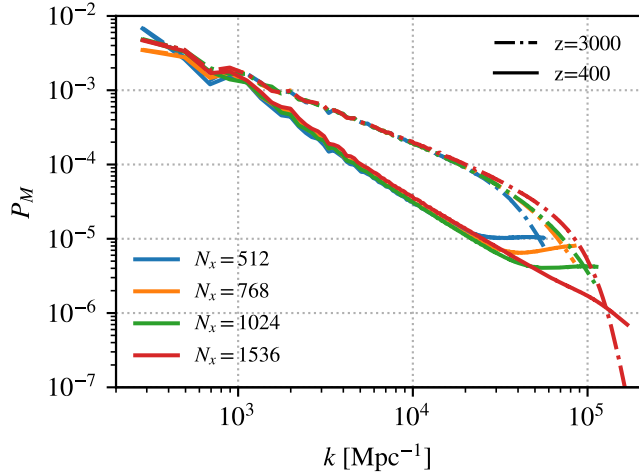


Figure B2. Magnetic power spectra at early ($z = 3000$) and late ($z = 400$) times for simulation runs with different resolution.

two lowest resolution runs with $N = 512^3$ and $N = 768^3$ showing a slight deviation from our *fiducial* run with $N = 1536^3$.

In Fig. B2 we show the power spectra of these different runs at early times $z = 3000$ as well as late times $z = 400$. The initial spectra differ slightly from each other since we start the simulation at $z > 3000$ and have a *ring-in* phase that is not shown here. The two runs with highest resolution converge reasonably well. For the runs with lower resolution there is a pile-up of magnetic power at $k \approx k_{\text{Ny}}$. This is the so-called bottleneck effect and shows that energy is not dissipated fast enough and the viscosity pre-factor ν_3 should be higher, for that particular resolution, to increase dissipation. For our chosen highest resolution of $N = 1536^3$, this bottleneck does not occur at a significant level and we obtain a power-law spectrum over all scales.